



# **Measurement of Something**

by

Kiyotaka Akabori

Submitted in partial fulfillment of the

requirements for the degree of

Doctor of Philosophy

at

Carnegie Mellon University

Department of Physics

Pittsburgh, Pennsylvania

Advised by Professor John F. Nagle  
and Professor Stephanie Tristram-Nagle

July 10, 2014







# Contents

<b>1</b>	<b>Introduction</b>	<b>1</b>
<b>2</b>	<b>Structural Perturbation of Lipid Bilayers Due to Tat Peptide</b>	<b>3</b>
2.1	Introduction . . . . .	3
2.2	Materials and Methods . . . . .	6
2.2.1	Stock Solutions . . . . .	6
2.2.2	Thin Film Samples . . . . .	6
2.2.3	Volume Measurements . . . . .	7
2.2.4	X-ray setup . . . . .	9
2.2.5	Analysis of Diffuse Scattering . . . . .	9
2.2.6	Modeling the Bilayer Structure . . . . .	15
2.2.7	Molecular Dynamics Simulation . . . . .	21
2.3	Analysis of Molecular Dynamics Simulation Data . . . . .	24
2.3.1	SIMtoEXP program . . . . .	24
2.3.2	Local Thinning of Membranes . . . . .	24
2.3.3	Lateral Decay Length of Membrane Thinning . . . . .	26
2.4	Results . . . . .	28
2.4.1	Bending and Bulk Modulus . . . . .	28
2.4.2	Volume results . . . . .	30
2.4.3	Electron Density Profile Modeling . . . . .	31
2.4.4	Hard Wall Constrain Fits . . . . .	41
2.4.5	Summary of Electron Density Profile Modeling . . . . .	42
2.4.6	Molecular Dynamics Simulations . . . . .	44
2.5	Discussion . . . . .	53
2.6	Conclusion . . . . .	56

<b>3 Ripple Phase</b>	<b>58</b>
3.1 Introduction . . . . .	58
3.2 Materials and Methods . . . . .	62
3.2.1 Sample Preparation . . . . .	62
3.2.2 Instrumental Resolution . . . . .	63
3.2.3 Low Angle X-ray Scattering Experiment . . . . .	71
3.2.4 Near Grazing Incidence Wide Angle X-ray Scattering Experiment	72
3.2.5 Transmission Wide Angle X-ray Scattering Experiment . . . . .	72
3.3 LAXS: analysis . . . . .	77
3.3.1 Lattice Structure . . . . .	77
3.3.2 Sample q-space . . . . .	78
3.3.3 Lorentz Correction . . . . .	80
3.3.4 Absorption Correction for LAXS . . . . .	85
3.3.5 Correction due to mosaic spread . . . . .	89
3.4 LAXS: model . . . . .	93
3.4.1 Contour Part of the Form Factor . . . . .	93
3.4.2 Transbilayer Part of the Form Factor . . . . .	93
3.5 LAXS: results . . . . .	97
3.5.1 Data and Electron Density Profile . . . . .	97
3.6 NGIWAXS: results . . . . .	103
3.7 TWAXS: results . . . . .	112
3.8 Discussion . . . . .	117
3.9 Conclusion . . . . .	118
<b>Appendices</b>	<b>120</b>
<b>A Tat</b>	<b>119</b>
A.1 Analysis of Fixed Angle Data using NFIT . . . . .	119
A.1.1 Theory . . . . .	119
A.1.2 Results . . . . .	119
A.2 Mosaic Spread for NFIT analysis . . . . .	119
A.2.1 Mosaic Spread: Calculation . . . . .	119
A.2.2 Mosaic Spread: Near Equivalence of Two Methods . . . . .	124
A.2.3 NFIT . . . . .	126
A.2.4 Results . . . . .	127

A.3	Some More Details of Tat Stuff if needed . . . . .	127
<b>B</b>	<b>Ripple Phase</b>	<b>128</b>
B.1	Derivation of the contour part of the form factor . . . . .	128
B.2	Rotation of a Two-Dimensional Function . . . . .	130
B.3	Derivation of the transbilayer part of the form factor in the 2G hybrid model . . . . .	131
B.4	Correction due to refractive index . . . . .	133

# List of Tables

2.1	Some Amino Acids Data . . . . .	8
2.2	Number of electrons per lipid and volume per lipid. . . . .	20
2.3	Some structural parameters for each component. $n_i^e$ is the number of electrons and $\rho_i$ is the average electron density. . . . .	20
2.4	Tat basic structural parameters. The notations are the same as in Table 2.3. $x_{\text{Tat}} = \text{Tat}/(\text{Tat}+\text{Lipid})$ . . . . .	20
2.5	Volume results at 37 °C . . . . .	31
2.6	Fitting Results for DOPC membranes for the THG (Tat in headgroup) model. $z_{\text{PC}} - z_{\text{CG}} = 3.1 \text{ \AA}$ and $z_{\text{CG}} - z_{\text{HC}} = 1.3 \text{ \AA}$ in all fits. . . . .	32
2.7	Fitting Results for DOPC:DOPE (3:1) membranes for the THG model. $z_{\text{PC}} - z_{\text{CG}} = 3.1 \text{ \AA}$ and $z_{\text{CG}} - z_{\text{HC}} = 1.3 \text{ \AA}$ in all fits. . . . .	35
2.8	(Numbers are wrong) Fitting Results for DOPC:DOPE (1:1) membranes for the THG model. $\Delta z_1 = z_{\text{PC}} - z_{\text{CG}}$ and $\Delta z_2 = z_{\text{CG}} - z_{\text{HC}}$ . . . . .	35
2.9	Fitting Results of the bound THG model for DOPC membranes. $\Delta z_1 = z_{\text{PC}} - z_{\text{CG}}$ and $\Delta z_2 = z_{\text{CG}} - z_{\text{HC}}$ . . . . .	42
2.10	Comparison of the simulated form factors to the experimental form factors. . . . .	49
2.11	Summary of simulation results. $\langle D_{\text{PP}} \rangle$ , phosphorus-phosphorus distance averaged over all lipids; $D_{\text{PP}}$ , Tat-perturbed phosphorus atoms; $x$ , thickness away from Tat; $\Delta t$ , $\langle D_{\text{PP}}^{\text{DOPC}} \rangle - D_{\text{PP}}$ ; $H_{\text{Tat}}$ , Tat height; $R_{\text{Tat}}$ , radius of Tat cylinder; $R_2$ , radius of the calculated in-plane Tat-perturbed region; $R_3$ , effective radius of the simulation box. . . . .	50
2.12	Summary of weighted average results. The caption is the same as Table 2.11. . . . .	50

3.1	Lattice constants for DMPC at $T = 18.0$ °C reported by Wack and Webb [8]. The data collected and analyzed in this thesis are colored blue. . . . .	61
3.2	Beam divergence . . . . .	63
3.3	Energy dispersion . . . . .	64
3.4	Geometric broadening . . . . .	70
3.5	Definitions of $Z_{\text{CH}_2}$ and $Z_{\text{W}}$ . . . . .	95
3.6	Observed intensity for $h = 1$ to 3 at $D = 57.8$ , $\lambda_r = 145$ , and $\gamma = 98.2^\circ$ . *Unoriented data are from Wack and Webb [8]. . . . .	98
3.7	Observed intensity for $h = 4$ to 9 at $D = 57.8$ , $\lambda_r = 145$ , and $\gamma = 98.2^\circ$ (continued from Table 3.6). . . . .	99

# List of Figures

1.1	Experimental phase diagram of DMPC from Ref. [11]. . . . .	2
2.1	LAXS of DOPC:DOPE (1:1) with $x_{\text{Tat}} = 0.034$ at 37 °C. White lobes of diffuse scattering intensity have large grey numbers, while lamellar orders and beam are shown to the left of the molybdenum beam attenuator (short, dark rectangle). $q_z$ and $q_r$ are the cylindrical coordinates of the sample $q$ -space, where $q_z$ -axis is along the bilayer normal and $q_r$ -axis is along the in-plane direction. The lamellar repeat spacing was $D = 66.2 \text{ \AA}$ . . . . .	10
2.2	Schematic of an oriented stack of lipid bilayers. Thick green curves represent an instance of thermally fluctuating bilayers. The dashed lines show the thermally averaged positions $z = nD$ of the centers of each bilayer and $u_n(x, y)$ gives the instantaneous deviation from the average. Each bilayer extends in the $\mathbf{r} = (x, y)$ plane. . . . .	11
2.3	Expanded view of a fluctuating bilayer. Along the two black solid lines, the electron density profile is identical in an incompressible bilayer. Along the dashed line, the bilayer appears thicker by a factor $1/\cos \alpha$ . This apparent thickness variation along the $z$ direction is corrected by the undulation correction. . . . .	12
2.4	Schematic of DOPC showing each lipid component. The dash lines show where the lipid is divided into different components. The lipid headgroup is divided into two components, phophate-choline (PC) and carbonyl-glycerol (CG). The hydrocarbon chain region is also divided into two components, methylene+methine ( $\text{CH}_2+\text{CH}$ ) and terminal methyl groups ( $\text{CH}_3$ ). . . . .	16
2.5	A model electron density profile for DOPC with Tat. . . . .	17

2.6 Our simple model to extract the local bilayer thickness from simulation trajectories. Tat is modeled as a cylinder with its height $H_{\text{Tat}}$ and radius $R_{\text{Tat}}$ . The local thickness is defined as $D'_{\text{phos-phos}}$ . The thickness of the unperturbed DOPC bilayer is $D_{\text{phos-phos}}$ . Blue highlighted lipids fall within the imaginary cylinder extended from the Tat. Unperturbed lipids are highlighted in green. . . . .	25
2.7 Simple model of the lateral decay of the membrane thickness perturbation due to Tat. . . . .	27
2.8 Bilayer bending modulus, $K_c$ , vs. Tat mole fraction $x_{\text{Tat}}$ . $D$ -spacings for DOPC/Tat mixtures varied from 64 to 68 Å, for DOPC/DOPE/Tat mixtures from 64 to 69 Å, for DOPC/DOPS/Tat (3:1) mixtures from 57 Å to 100 Å (pure DOPS was unbound), and for nuclear mimic/Tat mixtures from unbound (nuclear mimic) to 64 Å. Estimated uncertainty in all values is about $\pm 2$ . . . . .	29
2.9 Form factors of lipid mixtures (arbitrarily scaled and vertically displaced) with increasing Tat mole fractions $x_{\text{Tat}}$ indicated on figure legends. Lipid mixtures: A. DOPC B. DOPC/DOPE (3:1) C. DOPC/DOPE (1:1) D. DOPC/DOPS (3:1) E. Nuclear mimic. The entire $q_z$ range is shown in C, while others show partial ranges. Solid vertical lines indicate the $q_z$ values where the form factors equal zero between the lobes of diffuse data. . . . .	30
2.10 The best fits to DOPC form factors (left) and the corresponding electron density profiles (right) with $x_{\text{Tat}} = 0, 0.016, 0.034$ , and $0.059$ (from top to bottom). . . . .	33
2.11 The best fits to DOPC:DOPE (3:1) form factors (left) and the corresponding electron density profiles (right) with $x_{\text{Tat}} = 0, 0.016, 0.034$ , and $0.059$ (from top to bottom). . . . .	34
2.12 The best fits to DOPC:DOPE (1:1) form factors (left) and the corresponding electron density profiles (right) with $x_{\text{Tat}} = 0, 0.016, 0.034$ , and $0.059$ (from top to bottom). . . . .	36
2.13 Modeling results for absolute electron density profiles and for the Tat location as a function of distance $z$ along the bilayer normal. A. DOPC B. DOPC:DOPE (3:1), and C. DOPC:DOPE (1:1). . . . .	37

2.14 A. Bilayer thickness, $D_{\text{PP}}$ ; B. Bilayer thickness, $D_{\text{HH}}$ ; C. Area/lipid, $A_L$ ; D. Twice the Tat location, $2z_{\text{Tat}}$ : all plotted vs. Tat mole fraction $x_{\text{Tat}}$ . Error bars are standard deviations from imposing Tat Gaussian widths, $\sigma_{\text{Tat}} = 2.5, 3.0$ or $3.5 \text{ \AA}$ . Inverted blue triangles connected with dotted line are results from MD simulations, averaging the best fits to the X-ray data for each parameter, with standard deviations shown. . . . .	39
2.15 $\chi^2$ as a function of $z_{\text{Tat}}$ for DOPC, DOPC:DOPE (3:1), and DOPC:DOPE (1:1) (from left to right) with $x_{\text{Tat}} = 0.016, 0.034$ , and $0.059$ (from top to bottom). $\sigma_{\text{Tat}} = 3.0$ . The THG model (black squares) and the THC model (red circles). . . . .	40
2.16 $\chi^2$ as a function of $z_{\text{Tat}}$ for DOPC with $x_{\text{Tat}} = 0.016, 0.034$ , and $0.059$ (from top to bottom). $\sigma_{\text{Tat}} = 3.0$ . The bound THG model was used. . . . .	43
2.17 DPP graph with bound fits . . . . .	44
2.18 DHH graph with bound fits . . . . .	44
2.19 AL graph with bound fits . . . . .	44
2.20 zTat graph with bound fits . . . . .	44
2.21 MD simulated form factors for DOPC at $A_L = 68 \text{ \AA}^2$ (blue solid line), $70 \text{ \AA}^2$ (red solid line), and $72 \text{ \AA}^2$ (green solid line) compared to the experimental form factor (open circles) scaled vertically to best match the form factor for $70 \text{ \AA}^2$ . . . . .	45
2.22 The simulated, symmetrized electron density profile for DOPC at $A_L = 70 \text{ \AA}^2$ as a function of the distance away from the bilayer center. Each component profile is labeled with its name: PC (phosphate-choline), CG (carbonyl-glycerol), CH <sub>2</sub> +CH (methylene-methine combination), CH <sub>3</sub> (terminal methyl). The sum of all the components is labeled as total. . . . .	46
2.23 MD simulated form factors for DOPC with $x_{\text{Tat}} = 0.015$ at $A_L = 72 \text{ \AA}^2$ (top) and $74 \text{ \AA}^2$ (bottom), with $z_{\text{Tat}} = 18 \text{ \AA}$ (red solid lines), $16 \text{ \AA}$ (green solid lines), and $14 \text{ \AA}$ (blue solid lines) compared to the experimental form factor (open circles) scaled vertically to best match the form factor for $z_{\text{Tat}} = 18 \text{ \AA}$ . . . . .	47

2.24 MD simulated form factors for DOPC with $x_{\text{Tat}} = 0.030$ at $A_L = 74 \text{ \AA}^2$ (top) and $76 \text{ \AA}^2$ (bottom), with $z_{\text{Tat}} = 18 \text{ \AA}$ (red solid lines), $16 \text{ \AA}$ (green solid lines), and $14 \text{ \AA}$ (blue solid lines) compared to the experimental form factor (open circles) scaled vertically to best match the form factor for $z_{\text{Tat}} = 18 \text{ \AA}$ . . . . .	48
2.25 Electron density profiles of guanidinium groups from the four best matched simulations for DOPC with $x_{\text{Tat}} = 0.015$ (one Tat on each leaflet). Tat on the lower and upper leaflets are shown on the left and right plots, respectively. . . . .	51
2.26 MD simulated form factors (red solid lines in A and C) of Tat/(DOPC+Tat), $x_{\text{Tat}}=0.030$ , with Tat fixed at $z_{\text{Tat}}= 18 \text{ \AA}$ (panel A) and $5 \text{ \AA}$ (panel C) from the bilayer center compared to experimental form factors (open circles) scaled vertically to provide the best fit to the simulations. Corresponding snapshots are shown in Panels B and D in which the lipid chains are represented as grey sticks on a white background, Tats are yellow, phosphate groups are red and water is blue. . . . .	52
2.27 Location of Tat in DOPC bilayer. Tat is represented as a cylinder, $z$ is the distance from the bilayer center, and $R$ is the in-plane distance from the center of Tat. The average $z$ of the lipid phosphates as a function of $R$ and the arginine guanidiniums are shown in red and blue, respectively. . . . .	53
3.1 Lattice structure of the asymmetric ripple phase. Unit cells are shown in dash lines. Center of bilayers are shown by thick, solid lines. Notations in the figure are ( <b>a</b> and <b>b</b> : lattice unit vectors), ( $D$ : $D$ -spacing along $z$ ), ( $\lambda_r =  \mathbf{b} $ : ripple wavelength), ( $\gamma$ : oblique tilt angle), ( $A$ : ripple amplitude), ( $\psi$ : chain tilt angle with respect to the $z$ direction), and ( $x_M$ : projected length of the major arm). . . . .	59
3.2 Pictures of an annealing chamber . . . . .	62
3.3 The horizontal profile of the beam used in the 2013 low resolution study. Each pixel was 0.07113 mm, which gave a CCD angular resolution $\Delta\theta$ of $0.0057^\circ$ , corresponding to $\Delta q = 0.0011 \text{ \AA}^{-1}$ at the sample to detector distance of 359.7 mm. The beam FWHM = 1.7 pixels, giving $\Delta\theta = 0.010^\circ$ or $\Delta q = 0.0019 \text{ \AA}^{-1}$ . . . . .	65

3.4	The vertical profile of the beam used in the 2013 low resolution study. The beam height = 15 pixels = 1.1 mm. . . . .	65
3.5	In-plane geometric broadening due to the sample width $w_s$ and the beam width $\Delta x_{\text{beam}}$ . A top view of the sample (green) on the Si wafer (gray) and the incoming and diffracted X-rays (bounded by red solid lines) are shown. The total in-plane scattering angle for a lipid chain-chain correlation is labeled as $2\theta$ , and the geometric broadening as $\Delta x$ . . . . .	67
3.6	The horizontal profile of the beam used in the 2013 high resolution experiment. The CCD angular resolution $\Delta\theta = 0.0092^\circ$ corresponding to $\Delta q = 0.0017 \text{ \AA}^{-1}$ , at the sample to detector distance of 220.6 mm. The beam FWHM = 3.7 pixels = 0.26 mm, giving $\Delta\theta = 0.034^\circ$ or $\Delta q = 0.0063 \text{ \AA}^{-1}$ . . . . .	67
3.7	The vertical profile of the beam used in the 2013 high resolution experiment. The beam height = 9 pixels = 0.64 mm. . . . .	68
3.8	Geometric broadening in TWAXS . . . . .	69
3.9	Top and side view of the beam on the sample in TWAXS . . . . .	70
3.10	Projection of rectangular beam on the detector. Scattered beam appears as a parallelogram on the CCD. . . . .	70
3.11	(top panels) CCD images of X-ray scattering taken with (left) and without (right) a nominally 25 $\mu\text{m}$ thick Mo attenuator. These data were taken at a fixed angle of incidence $\omega = 0.8^\circ$ . The sample was an oriented film of DOPC:DOPE (3:1) in the fluid phase at 37 °C. The wavelength was 1.175 $\text{\AA}$ , the same as the one used for the ripple phase experiment. The same gray scale is used in both images. 100 pixel = 0.11 $\text{\AA}^{-1}$ in $q$ . A small dot located about $(p_x, p_z) = (520, 170)$ between the first and second orders is a specular reflection from the substrate. The exposure times were 1 second. (bottom panels) Vertical $p_z$ slices of the X-ray images shown in the top panels (left). The scattering intensity measured with the attenuator (red solid circles) was multiplied by a factor of 6.9 and compared to the intensity measured without the attenuator (black solid circles, right). . . . .	73

3.12 1 second exposure (left) and 60 second exposure (right) of the low angle X-ray scattering from the DMPC ripple phase in gray log scales. The index $h$ is labeled in green. $(3, k)$ reflections are identified in cyan. The shadow cast by 100 $\mu\text{m}$ thick molybdenum attenuator blocking strong $(1,0)$ and $(2,0)$ orders in the right image is labeled as attenuator and extends from $q_z = 0 \text{ \AA}^{-1}$ to $0.2 \text{ \AA}^{-1}$ . $D = 57.8 \text{ \AA}$ , $\lambda_r = 145.0 \text{ \AA}$ , and $\gamma = 98.2^\circ$ .	74
3.13 Schematics of the sample holder in the transmission mode. Side (left) and top (right) views are shown. The thickness of the Si wafer = 35 $\mu\text{m}$ . The thickness of the sample $\approx 10 \mu\text{m}$ . The distance between the axis of rotation and sample = 21.1 mm.	75
3.14 Circular path followed by the sample as the angle of incidence $\omega$ was changed. The sample to detector distance and $D$ -spacing of the sample were measured in the LAXS mode, where $\omega = 1^\circ$ . WAXS images were collected at the transmission mode, where $\omega = -45^\circ$ . The $z$ position of the sample was slightly higher at the LAXS mode than at the transmission mode, so the sample holder was vertically shifted for different modes.	76
3.15 Picture of the sample holder looking from above. A lead tape was attached to the back of the sample holder to help reduce the background scattering, typically coming from the air gap between the flightpath snout and the mylar window of the chamber.	76
3.16 Experimental reflectivity geometry.	79
3.17 Ewald sphere construction for the ripple phase diffraction in the low angle regime. A ripple $k = 0$ peak is the solid, black circle on the $q_z$ -axis. A ripple $k \neq 0$ ring is the black ring centered about the $q_z$ -axis. The portion of the ring that is inside the Ewald sphere is shown as a red dashed line and the portion of the ring that is outside but behind the Ewald sphere is shown as a black dotted line. The magnitude of the total scattering angle is exaggerated. With a wavelength of 1.175 $\text{\AA}$ , the magnitude $ \mathbf{k}_{\text{in}}  = 5.35 \text{ \AA}^{-1}$ . For a $h = 5$ peak, $q_{50}^z = 0.54 \text{ \AA}^{-1}$ , one tenth of $k_{\text{in}}$ .	81
3.18 Side view of an arc of $k = 0$ peak shown as a thick blue line.	82

3.19 $q$ -space representations of Bragg peaks and Bragg rings for $h = 1$ and $2$ and $k = 0, 1$ , and $2$ in $q_{hk}^z$ planes. The intersection between the Ewald sphere and a Bragg peak/ring is indicated in red. The observed intensity for the $k \neq 0$ orders is proportional to the fraction of the length of red arcs in the circumference. This fraction is equal to one for $k = 0$ reflections. Because the reflections are not in the same $q_z$ plane, the range of $q_y$ integration indicated by the height of the gray rectangle is different for different $h$ orders. For $\gamma \neq 90^\circ$ , the range of $q_y$ integration is slightly different for different $k$ reflections with the same $h$ . The values shown are for $D = 58 \text{ \AA}$ , $\lambda_r = 145 \text{ \AA}$ , $\gamma = 90^\circ$ , and $\lambda = 1.175 \text{ \AA}$ . The magnitude of curvature of arcs is exaggerated. . . . .	83
3.20 The path of X-rays within the sample. The incident angle is $\omega$ and the total scattering angle is $2\theta$ . An X-ray with a penetration depth of $z$ is shown. The total thickness of the sample is $t$ . Refraction correction is smaller than what? for $\theta > 0.5^\circ (h = 1)$ . . . . .	86
3.21 Absorption factors as a function of $q_z \approx 4\pi\theta/\lambda$ . Values at $q_z = 2\pi h/D$ corresponding to $D = 57.8 \text{ \AA}$ are shown as squares. $\mu = 2600 \text{ \mu m}$ , $t = 10 \text{ \mu m}$ , and $\lambda = 1.175 \text{ \AA}$ . . . . .	88
3.22 Eq. (3.30) plotted as a function of $\omega$ for $\theta = \theta_B$ . . . . .	89
3.23 Contours of a mosaic spread distribution projected on the $\omega\chi$ -plane, where $\chi - \chi_{hk}$ is an angle measured from a $(h, k)$ reflection on the detector ( $\chi = \pi/2 - \phi$ in Fig. 3.16) and $\theta_{hk}$ is the Bragg angle for a $(h, k)$ reflection. The distribution function takes a form of Lorentzian centered at $\alpha = 0$ . Domains with $\alpha = 0$ are probed at $\omega = \theta_{hk}$ and $\chi = \chi_{hk}$ . Integrated intensity of $(1, k)$ reflection arises from domains in the green shaded area while that of $(3, k)$ reflection is from the blue shaded area, which is three times larger. . . . .	90
3.24 Mosaic factor given by Eq. (3.37) as a function of $q_z \approx 4\pi\theta/\lambda$ . . . . .	92
3.25 title goes here . . . . .	94
3.26 Electron density profile calculated using the phases obtained from the M2G model and experimental form factors . . . . .	101
3.27 Electron density profile calculated using the phases obtained from the M2G model and experimental form factors . . . . .	102

3.28	NGIWAXS of the DMPC ripple phase for $D = 59.2 \text{ \AA}$ (left) and $60.8 \text{ \AA}$ (right). The angle of incidence $\omega$ was $0.2^\circ$ . The black regions around the edge of each image are the $q$ -space that was not probed. The distorted, non rectangular shape of the probed $q$ -space signifies non-linear relation between the CCD space and sample $q$ -space. . . . .	104
3.29	Enlarged view of the right image in Fig. 3.28. To show smaller features around the peak, a different contrast is used. . . . .	105
3.30	$q_r$ swath averaged over $0.02 \text{ \AA}^{-1}$ centered at $q_z = 0.20 \text{ \AA}^{-1}$ . . . . .	106
3.31	$q_r$ swath averaged over $0.02 \text{ \AA}^{-1}$ centered at $q_z = 0.12 \text{ \AA}^{-1}$ . . . . .	106
3.32	$q_r$ swaths, each averaged over $0.02 \text{ \AA}^{-1}$ . The center $q_z$ value of a swatch is shown in the figure legends. . . . .	107
3.33	NGIWAXS of the DMPC gel phase . . . . .	108
3.34	(left) NGIWAXS of the DMPC fluid phase at $30^\circ\text{C}$ . $\omega = 0.5^\circ$ . The data were taken in the 2011 run with a low resolution setup. The sample width, $w_s = 2 \text{ mm}$ . (right) NGIWAXS of the DMPC ripple phase at $18^\circ\text{C}$ . $\omega = 0.2^\circ$ . The data were also taken in 2011 with a low resolution setup. $w_s = 2 \text{ mm}$ . . . . .	109
3.35	$q_r$ swaths comparing intensity of the fluid WAXS and ripple WAXS. The fluid phase data were scaled so that its WAXS lies below the ripple WAXS. . . . .	110
3.36	Subtraction of the fluid phase WAXS from the ripple phase WAXS. The subtraction results in asymmetric ripple peak. . . . .	111
3.37	TWAXS image of the DMPC ripple phase . . . . .	113
3.38	$q_r$ swath of the TWAXS image averaged over $0.02 \text{ \AA}^{-1}$ centered at $q_z = 0.12 \text{ \AA}^{-1}$ . . . . .	114
3.39	$q_r$ swaths of the TWAXS image, each averaged over $0.02 \text{ \AA}^{-1}$ . The center $q_z$ value of a swatch is shown in the figure legends. . . . .	115
3.40	$q_z$ swath averaged between $1.46 \text{ \AA}^{-1}$ and $1.52 \text{ \AA}^{-1}$ . . . . .	116
A.1	Two dimensional view of mosaic spread (left) and notations used in this section (right). The stacking direction of an ideal domain is $\mathbf{n}$ and that of a tilted domain $\mathbf{n}'$ . The deviation of $\mathbf{n}'$ from $\mathbf{n}$ denoted as $\alpha$ quantifies the degree of misorientation of a domain. The $x$ , $y$ , and $z$ -axes are the sample coordinates. . . . .	120

A.2 Example of a two dimensional sample consisting of an ideal and tilted domains. $\mathbf{q} = (q_x, q_z)$ is the sample $q$ -space and $\mathbf{q}' = (q'_x, q'_z)$ is the domain $q$ -space. The two $q$ -spaces are related by a rotation of $\alpha$ about the $y$ -axis, which is into the page. . . . .	121
A.3 Notations used in this section. The arc originating from the $Z$ -axis is the mosaic arc due to the mosaic spread distribution. . . . .	124
A.4 Rocking scan trace in $q$ -space. . . . .	125

# Chapter 3

## Ripple Phase

When the temperature is reduced from the fluid phase, the ripple phase is observed in bilayers consisting of DMPC and DPPC lipids. This chapter discusses X-ray scattering experiments on the ripple phase formed by dimyristolphosphatydylcholine (DMPC) bilayers.

### 3.1 Introduction

(At some point, do some literature search and write up this section) The ripple phase has been a fascinating thermodynamic phase to many physicists and physical chemists since its discovery. It was originally observed in calorimetry study for alkanes by sturevant. Although this phase has never been reported to occur in a biologically relevant situation, it provides an interesting opportunity to study fundamental lipid interactions and their influence on the bilayer shape. (Let's find some recent papers and see if anyone says anything about biological relevance)

In the first structural study of this phase by Tardieu *et al.*, the X-ray diffraction pattern from DLPC was phased by a pattern recognition technique and the electron density map was calculated. It was shown that the structure corresponds to a 2D oblique unit cell shown in Fig. 3.1. The calculated electron density map showed that DLPC bilayers are height modulated and have a smooth, asymmetric shape. The ripple wavelength  $\lambda_r$  was reported to be 85.3 Å, the lamellar periodicity  $D$  55.3 Å, and the oblique angle  $\gamma$  110°. The electron density map reported the ripple amplitude  $A = 15$  Å in DLPC.

Various experiments have indicated the existence of two types of ripple phases: the

stable asymmetric and the metastable symmetric phase. In the asymmetric phase, a plane of reflection perpendicular to the ripple wave vector is absent. The metastable symmetric phase has been seen in DPPC bilayers, but not in DMPC.

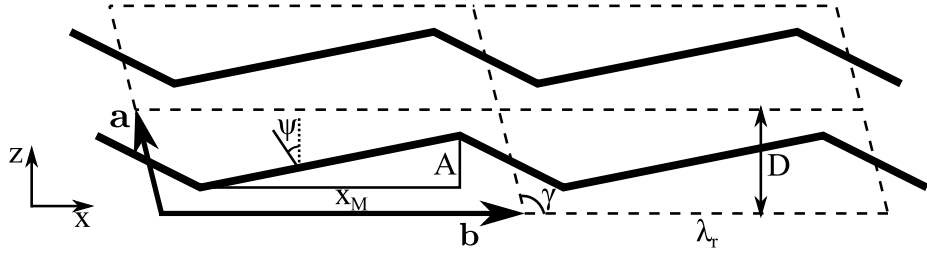


Figure 3.1: Lattice structure of the asymmetric ripple phase. Unit cells are shown in dash lines. Center of bilayers are shown by thick, solid lines. Notations in the figure are (**a** and **b**: lattice unit vectors), ( $D$ :  $D$ -spacing along  $z$ ), ( $\lambda_r = |\mathbf{b}|$ : ripple wavelength), ( $\gamma$ : oblique tilt angle), ( $A$ : ripple amplitude), ( $\psi$ : chain tilt angle with respect to the  $z$  direction), and ( $x_M$ : projected length of the major arm).

The equilibrium structure of the ripple phase has been extensively studied by X-ray diffraction [2, 8, 11, 85–88], neutron diffraction [89, 90], AFM [], freeze fracture electron microscopy [91], and freeze fracture scanning tunneling microscopy [] techniques. In the scanning tunneling microscopy experiment [7], the three-dimensional contours of the ripple phase  $P_{\beta'}$  of dimyristoylphosphatidylcholine (DMPC) were imaged, and a ripple wavelength of 130 Å and an amplitude of 45 Å were reported.

Some argued that inter-membrane interactions are important in mechanism of the ripple phase formation (REF?). However, the ripple phase was also found in unilamellar vesicles, where a vesicle has only one bilayer [?].

The ripple phase has been detected in a wide variety of lipids, including phosphatidylcholines, phosphatidylacetoyl (PA), and phosphatidylglycerol (PG), but no ripple phase has been observed in bilayers composed of PE headgroups. These studies suggest that the size of headgroup has something to do with the ripple formation.

From X-ray data of the DMPC ripple of unoriented samples, Wack and Webb [8] argued that the ripples have a sawtooth shape, but were unable to phase the observed pattern. Their X-ray form factor data were later phased by employing a modeling and fitting technique by Sun *et al.* [87], and the electron density map was calculated, which indicated that the ripples indeed have a sawtooth shape. The map also showed that the major arm is about twice as long as the minor arm. The bilayer thickness was found to be larger than that of the minor arm. The value of the bilayer thickness

in the major arm was comparable to the thickness of DMPC bilayers in the gel phase whereas the thickness of the minor arm was comparable to that in the fluid phase.

A structural investigation by X-ray diffraction of the ripple phase of oriented dipalmitoylphosphatidylcholine (DPPC) samples indicated that hydrocarbon chains are packed in a hexagonal lattice with chains tilted in the plane perpendicular to the ripple wave vector [92]. In that study, the oblique angle  $\gamma$  was found to be  $90^\circ$ . It is believed that the resolved structure was for the symmetric ripple, which has been shown to be thermodynamically metastable and whose occurrence depends on the sample history [93]. In [92], only symmetric ripple was observed in the low angle X-ray scattering, which seems to contract with the metastability of this symmetric ripple.

**Katsaras and Raghnathan papers** Sengupta et al. investigated temperature dependence of the average structure of DMPC and concluded that there is no obvious change in the structure as a function of temperature. On the other hand, the ripple phase composed of POPC showed some variation in the average structure. Based on calculated electron density profiles and model parameters, they argued that chains in both major and minor arms are tilted with respect to the  $z$  direction by the same amount and in the major arm chains are parallel to the local normal. This speculation is inconsistent with the findings in [87] that the thickness of major arm is almost identical to that of the gel phase where chains are tilted by  $\sim 30^\circ$ . To accomodate this discrepancy, Sengupta et al. aruged that chains might be titled by some amount into the direction perpendicular to the ripple direction, but this type of information is not well captured in the low angle scattering data. From these studies, it is clear that wide angle scattering data are necessary.

In a giant unilamellar vesicle composed of a mixture of DPPC and DOPC, co-existing domains of  $L'_\beta$  and  $P'_\beta$  have been found [94]. The  $P'_\beta$  domain had lower concentration of DPPC than the  $L'_\beta$  domain. Addition of anionic lipids (DOPG?) turned the gel phase domain into the ripple phase domains. The authors concluded that reduction of surface tension drove highly stressed gel phase to less stressed ripple phase.

**AFM** The ripple phase has also been observed in the top layer of solid supported double layers through atomic force microscopy (AFM). The effect of the bottom layer on the top layer in the ripple phase has not been thoroughly studied. It is not clear whether the structure of these ripple formation top layers is the same as that in a

bulk sample such as MLVs and oriented samples.

Several MD (molecular dynamics) simulations have shed light on molecular organization in the ripple phase as well. de Vrie *et al.* carried out atomistic simulations resulting in an assymetric ripple where chains are gel-like in the major arm and interdigitated in the minor side [95]. Coarse-grain simulations essentially found the same results.

### Some theory papers. What causes ripple phase?

$D$ (Å)	$\lambda_r$ (Å)	$\gamma$ (deg)
55.0	159.4	99.0
57.0	140.8	97.6
57.3	151.6	97.8
57.4	148.4	97.6
57.5	144.1	97.8
57.5	141.9	98.0
58.0	140.1	98.2
<b>57.8</b>	<b>145.0</b>	<b>98.2</b>
58.0	141.7	98.4
59.8	129.6	97.3
60.6	130.1	97.0
61.5	130.8	96.5
62.4	122.0	95.9
63.9	123.1	94.9
64.9	120.3	92.3

Table 3.1: Lattice constants for DMPC at  $T = 18.0\text{ }^\circ\text{C}$  reported by Wack and Webb [8]. The data collected and analyzed in this thesis are colored blue.

## 3.2 Materials and Methods

### 3.2.1 Sample Preparation

DMPC was purchased from Avanti Polar Lipids. Four mg DMPC powder was dissolved in 140  $\mu\text{l}$  chloroform:methanol (2:1 v:v) mixture. The solution was plated onto silicon wafers following the rock and roll procedure [96]. See also Sec. 2.2.3. For all the ripple phase experiments, the temperature of the hydration chamber was set to 18 °C. In 2011 and 2012 synchrotron experiments, the samples were created and annealed more than a week in advance and stored in a refrigerator. The quality of these samples measured by their mosaic spread was found to worsen over time after the samples were annealed. Therefore, to attempt better quality, the samples were annealed for only about 12 hours just before the X-ray experiment. Figure 3.2 shows a picture of the annealing chamber. Annealing is promoted both by hydration and by elevated temperature. To achieve gentle but efficient hydration of a sample, filter papers were installed that exposed a larger surface for evaporation. The temperature was set to 60 °C. It must be emphasized that the annealing chamber should equilibrate in an annealing oven set to 60 °C, prior to putting a sample in the chamber. When a sample was put in the chamber sitting at a room temperature and then the system was placed inside the oven, warmer water vapor inside the chamber condensed on the cooler sample, causing so called flooding of oriented sample. A small drop of water on an oriented film is detrimental for the orientation quality because the entropy-driven formation of unilamellar vesicles causes oriented bilayers to peel off one by one.

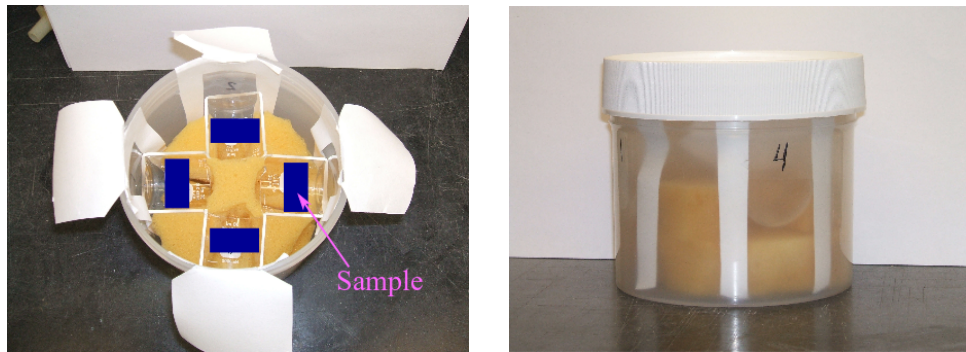


Figure 3.2: Picture of an annealing chamber.

The sample for the grazing incident wide angle study was prepared in the same way as for low angle study. In order to minimize the geometric broadening, the sample

was trimmed to 1 mm in width along the beam direction.

The sample for transmission study was deposited on a thin, 35 micron, silicon wafer, and oriented following the rock and roll procedure [96]. Because the wafer was very fragile, attaching the sample to a sticky thing was impossible. Instead, the sample was attached to a plastic cap on a small vial with a small amount of heat sink compound at a corner of the wafer. The wafer was stable enough for rocking.

### 3.2.2 Instrumental Resolution

The X-ray scattering experiments were carried out at the Cornell High Energy Synchrotron Source (CHESS) G1 station in three different runs (2011, 2012, and 2013). The low angle X-ray scattering (LAXS) data analyzed in this thesis were collected in 2013. The near grazing incidence wide angle X-ray scattering (NGIWAXS) data were also collected in the 2013 run, but with smaller energy dispersion than in the LAXS experiment. The transmission wide angle X-ray scattering (TWAXS) data were collected in the 2011 run. The ripple phase experiment in the 2012 run was not successful due to low sample quality. The instrumental resolution in these X-ray experiments depended on the beam divergence, energy dispersion, and geometric broadening.

#### Divergence

The beam divergence quantifies an angular spread of the incoming X-ray beam. We estimated the beam divergence by measuring the horizontal and vertical beam widths at two known sample-to-detector  $S$  distances with difference  $\Delta S$ . The beam widths were larger at the further distance, which indicated that the beam was divergent. We calculated the divergence as  $\text{div} = \Delta B / \Delta S$ , where  $\Delta B$  is the difference in beam widths at different  $S$  distances. Table 3.2 summarizes beam divergence.

year	type of experiment	horizontal (rad.)	vertical (rad.)
2013	LAXS	$4.2 \times 10^{-5}$	$1.6 \times 10^{-4}$
2013	NGIWAXS	$4.2 \times 10^{-5}$	$1.6 \times 10^{-4}$
2011	TWAXS	$2.5 \times 10^{-5}$	$5 \times 10^{-5}$

Table 3.2: Beam divergence

## Energy dispersion

A W/B<sub>4</sub>C multilayer monochromator with energy bandwidth  $\Delta E/E$  of 1.3% was used in the LAXS and TWAXS experiments. The energy of the X-ray beam was 10.55 keV, corresponding to a wavelength  $\lambda$  of 1.175 Å, in the LAXS experiment. To achieve a higher instrumental resolution than that for the LAXS experiment, a (111) silicon monochromator was used for the NGIWAXS experiment, which gave  $\Delta E/E$  of 0.01%. Due to the geometry of the G1 station, the Si monochromator was placed in the G1 hutch, in series with the multilayer monochromator. Table 3.3 summarizes energy dispersion.

year	type of experiment	$\Delta E/E$ (%)	$E$ (keV)	$\lambda$ (Å)
2013	LAXS	1.5	10.55	1.175
2013	NGIWAXS	0.01	10.55	1.175
2011	TWAXS	1.5	10.54	1.176

Table 3.3: Energy dispersion

## Geometric Broadening

The beam footprint on the sample has a finite size and this causes geometric broadening of diffraction peaks on the CCD detector.

**LAXS** In the LAXS experiment, the geometric broadening in the horizontal  $x$  direction is simply the horizontal beam width for  $k = 0$  peaks with minor additional broadening for  $k \neq 0$  peaks. Geometric broadening in the vertical  $z$  direction is due to different heights of the sample along the  $y$  direction of the beam at non zero angle of incidence  $\omega$ . It is given approximately by  $w_s \tan \theta$ , where  $w_s$  is the sample width along the  $y$  direction and  $\theta$  is the scattering angle. The beam shape, measured through a semi-transparent 200 µm thick molybdenum (Mo) beam stop, is shown in Fig. 3.3 and 3.4. The horizontal beam width was 1.7 pixels (0.12 mm). The vertical beam width was approximately 1 mm, tall enough to cover the entire sample if the sample was tilted between 0° and 11.5°. The sample was rocked during X-ray exposure between -1.6° and 7° in order to observe many diffraction peaks in one data collection and keep all the sample in the beam.

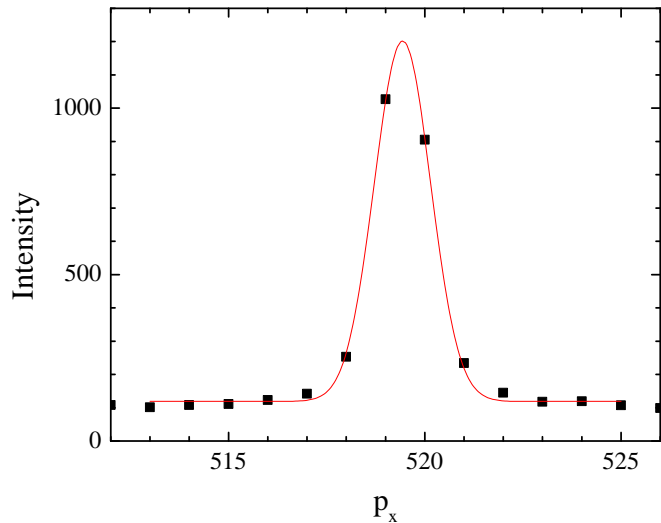


Figure 3.3: The horizontal profile of the beam used in the 2013 low resolution study. Each pixel was 0.07113 mm, which gave a CCD angular resolution  $\Delta\theta$  of 0.0057°, corresponding to  $\Delta q = 0.0011 \text{ \AA}^{-1}$  at the sample to detector distance of 359.7 mm. The beam FWHM = 1.7 pixels, giving  $\Delta\theta = 0.010^\circ$  or  $\Delta q = 0.0019 \text{ \AA}^{-1}$ .

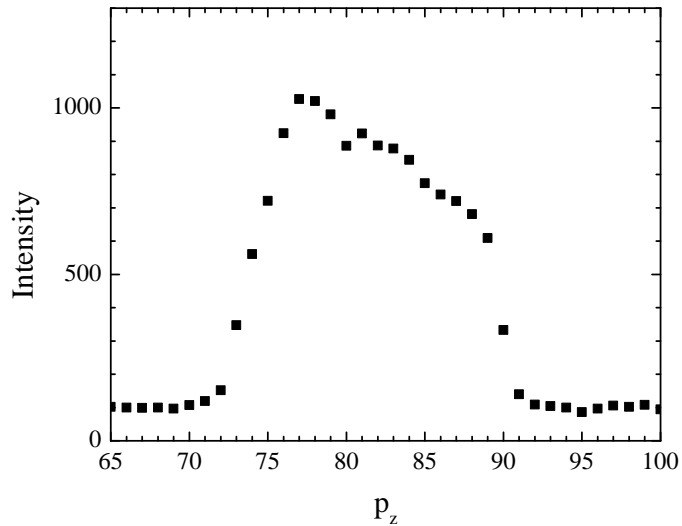


Figure 3.4: The vertical profile of the beam used in the 2013 low resolution study. The beam height = 15 pixels = 1.1 mm.

**NGIWAXS** In the NGIWAXS experiment, the horizontal geometric broadening was due to the sample width along the beam direction and the horizontal beam width. From the geometry of the experiment shown in Fig. 3.5, the geometric broadening  $\Delta x$  can be estimated, assuming simple additivity,

$$\Delta x = \Delta x_{\text{beam}} + w_s \tan(2\theta),$$

where  $\theta$  is the in-plane scattering angle. The total scattering angle  $2\theta$  for the ripple WAXS was approximately  $16^\circ$ . To minimize the contribution to  $\Delta x$  from the sample, the sample was trimmed to  $w_s = 1$  mm along the beam direction. This width was chosen because (1) I could not trim more without a more sophisticated device than a simple razor blade, (2) a very narrow sample would be a weak scattering body, and (3) disordering effect from the sample edge might become too significant to ignore. Given the above reasons and due to limited availability of synchrotron beam time, I considered a 1 mm width to be reasonable. The horizontal beam width was 4 pixels (0.28 mm) as shown in Fig. 3.6. With these experimental parameters, the resolution was estimated to be  $\Delta x = 0.57$  mm = 8 pixels, which would be the unresolved width of an intrinsically infinitely sharp wide angle peak. [Comment and refer to the gel phase data shown in the result section of NGIWAXS.](#) The sample to detector distance were 220.6 mm, measured using silver behenate. Then, the minimum peak width measured in  $q$ -space would be  $\Delta q \approx 0.014 \text{ \AA}^{-1}$ . The vertical geometric broadening was negligible because the sample width  $w_s$  was narrow and scattering of interest occurred at small  $q_z$ .

**TWAXS** In the TWAXS experiment, geometric broadening in both  $x$  and  $z$  directions was non-negligible. To calculate the broadening, let us assume that the beam has a rectangular cross section with its height  $Y_b$  and width  $X_b$  as shown in Figure 3.8. When the sample is tilted by  $\omega$ , X-rays emerging from the top edge of the sample travel extra distance compared to the distance that X-rays from the bottom edge of the sample travel. This, then, leads to distortion of the scattered beam; namely, the scattered beam will appear on the CCD screen as a parallelogram as shown in Figure 3.8. Figure 3.9 shows the top- and sideview of the projection of the beam on the sample. From simple geometry, it can be shown that  $a = Y_b / \tan \omega$ ,  $b = aX/(2S)$ ,  $c = aZ/(2S) + Y_B/2$ , and  $B = \tan^{-1}(Z/S)$ . Since  $H = 2c$  and  $W = 2b$ ,  $H$  and  $W$  in

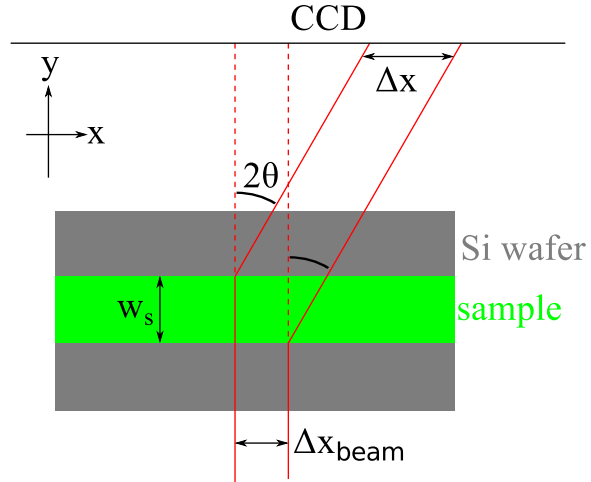


Figure 3.5: In-plane geometric broadening due to the sample width  $w_s$  and the beam width  $\Delta x_{beam}$ . A top view of the sample (green) on the Si wafer (gray) and the incoming and diffracted X-rays (bounded by red solid lines) are shown. The total in-plane scattering angle for a lipid chain-chain correlation is labeled as  $2\theta$ , and the geometric broadening as  $\Delta x$ .

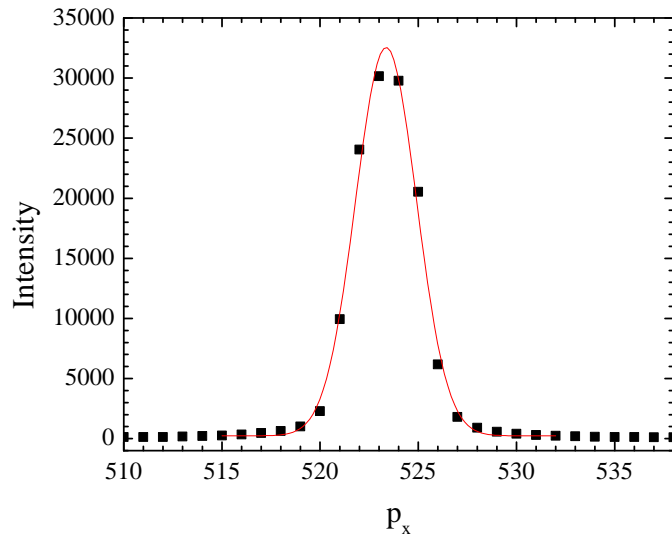


Figure 3.6: The horizontal profile of the beam used in the 2013 high resolution experiment. The CCD angular resolution  $\Delta\theta = 0.0092^\circ$  corresponding to  $\Delta q = 0.0017 \text{ \AA}^{-1}$ , at the sample to detector distance of 220.6 mm. The beam FWHM = 3.7 pixels = 0.26 mm, giving  $\Delta\theta = 0.034^\circ$  or  $\Delta q = 0.0063 \text{ \AA}^{-1}$ .

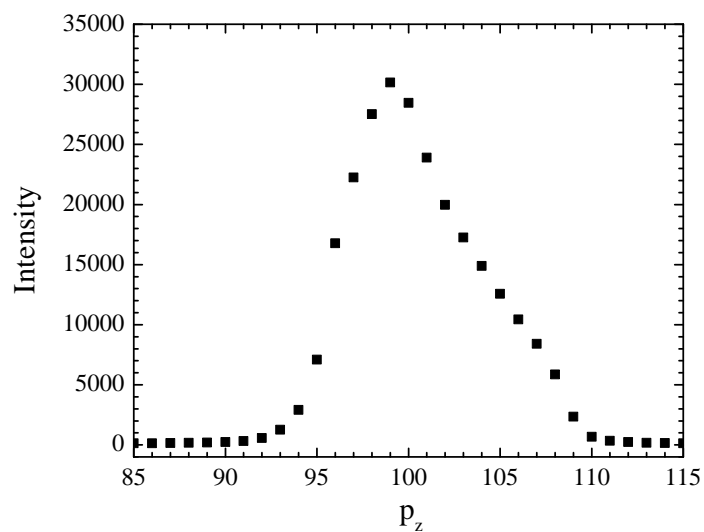


Figure 3.7: The vertical profile of the beam used in the 2013 high resolution experiment. The beam height = 9 pixels = 0.64 mm.

Figure 3.10 are given by

$$H = Y_b \left( 1 + \frac{Z}{S \tan \omega} \right) \quad (3.1)$$

$$W = Y_b \frac{X}{S \tan \omega}. \quad (3.2)$$

The sample to detector distance  $S$  was 158.6 mm, giving an angular CCD resolution of  $0.013^\circ/\text{pixel}$ , or  $0.0024 \text{ \AA}^{-1}/\text{pixel}$ . The observed wide angle peak was at  $(X, Z) = (44.0 \text{ mm}, 15.5 \text{ mm})$ . The beam width and height were both  $0.2 \text{ mm} = 2.8 \text{ pixels}$ . With this setup,  $W = 0.7 \text{ pixels}$  and  $H = 3.1 \text{ pixels}$ . Therefore, the distorted shape of the diffraction peak was negligible. Table 3.4 summarizes geometric broadening for our experiments.

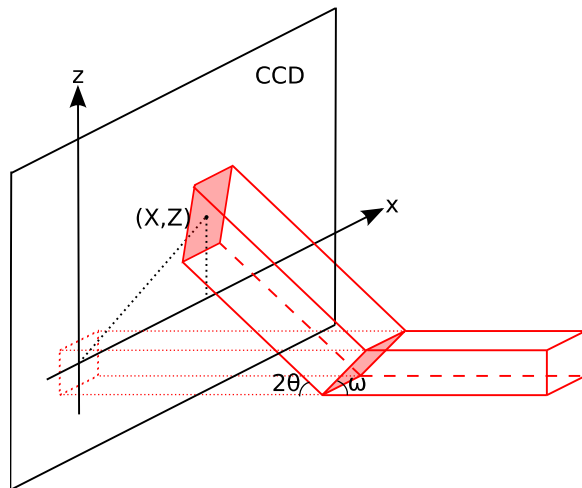


Figure 3.8: Geometric broadening in TWAXS. The cross section of the incoming X-ray with the sample and the CCD detector are both shaded in red. The sample is tilted by  $\omega$ . The red dots show the transmitted beam. The incoming beam is rectangular but upon scattering appears as a parallelogram on the CCD.

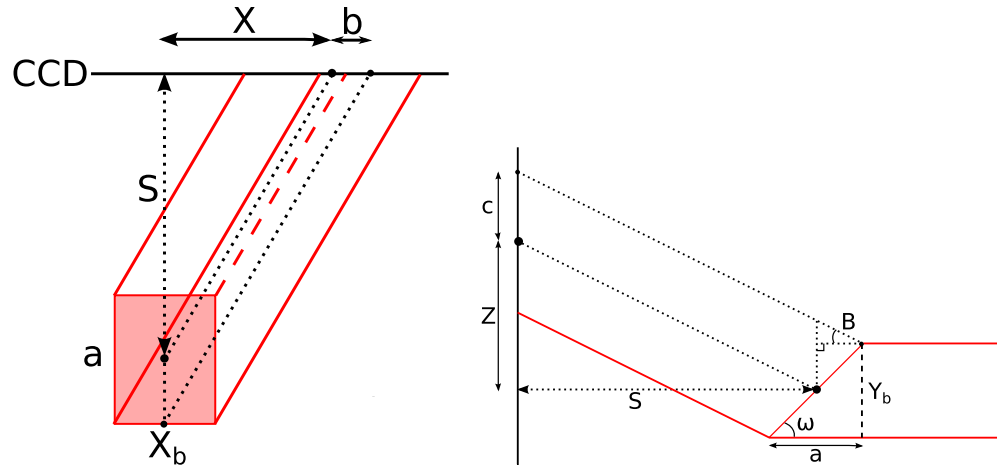


Figure 3.9: Top and side view of the beam on the sample in TWAXS. The cross section of the incoming X-ray with the sample is shaded in red.  $X_b$  and  $Y_b$  are the beam width and height, respectively.  $S$  is the sample to detector distance.  $(X, Z)$  is a position of the center of the scattered beam on the detector with respect to the center of the transmitted beam as shown in Figure 3.8.

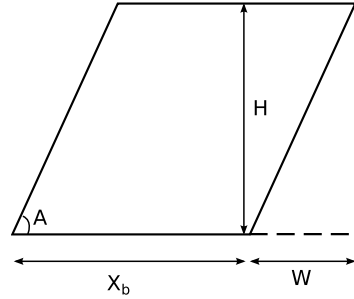


Figure 3.10: Projection of rectangular beam on the detector. Scattered beam appears as a parallelogram on the CCD.

type of experiment	horizontal (pixels)	horizontal ( $\text{\AA}^{-1}$ )	vertical (pixels)	vertical ( $\text{\AA}^{-1}$ )
LAXS	1.7	0.0019	$6.6q_z$	$0.0072q_z$
NGIWAXS	8	0.014		
TWAXS	2.8	0.0067	3.1	0.0074

Table 3.4: Geometric broadening

### 3.2.3 Low Angle X-ray Scattering Experiment

The X-ray beam for the low angle X-ray scattering (LAXS) experiment was set up by the station scientist, Dr. Arthur Woll. We chose the sample to detector distance to be 359.7 mm, measured by indexing silver behenate Bragg peaks. The D-spacing of silver behenate is known to be 58.367 Å.

Occasionally, sheets of molybdenum (Mo), each nominally 25  $\mu\text{m}$  were used to attenuate the incoming beam. These sheets were installed by Dr. Arthur Woll in the upstream of the sample chamber. The attenuation length  $\mu$  of 10.55 keV X-ray in Mo is 13.74  $\mu\text{m}$  [97]. For a 25  $\mu\text{m}$  thick Mo attenuator, the attenuation factor is calculated to be  $[\exp(-25/13.74)]^{-1} = 6.2$ . The exact attenuation factor was determined by comparing X-ray images collected with and without the attenuator, shown in Fig. 3.11 and ???. The attenuation factor of the nominally 25  $\mu\text{m}$  thick Mo was found to be 6.9 for the wavelength used (1.175 Å), indicating an actual thickness of 27  $\mu\text{m}$ .

Sheets of Mo were also used as a semi-transparent beam stop downstream of the sample, just outside the hydration chamber, to attenuate the beam and strong orders. 100 and 200  $\mu\text{m}$  were used to attenuate strong orders and either 200 or 225  $\mu\text{m}$  to attenuate the beam. To avoid saturation of CCD pixels by the very intense beam of  $10^{11}$  photons/mm<sup>2</sup>/second, the beam stop was always set to attenuate the beam.

A few Bragg peaks in the low angle X-ray scattering of the ripple phase were very strong, leading to saturation of CCD pixels for data collection with a long exposure time. In order to probe a wide range of  $q$ -space, three images were taken: 1) a short, one second exposure with a nominally 25 micron molybdenum attenuator installed in the upstream of the sample to reduce the intensity of the incoming X-ray beam, 2) one second exposure without the beam attenuator, and 3) 60 second exposure with a beam stop blocking the very intense (1,0) and (2,0) peaks. See Fig. 3.12. Then, the integrated intensity of (1,0) peak was measured from the first image. This value was multiplied by 6.9 to account for the beam attenuation and by 60 to scale with the exposure time. The intensity of (2,0) and (2,-1) were measured from the second image, also multiplied by 60 to account for the shorter exposure time. The intensities of the rest of the observed peaks were measured from the third image.

The integrated intensity of each peak was obtained using the Nagle lab tview software developed by Dr. Yufeng Liu [50] by putting a box around a peak and summing up the intensity in those pixels that fall inside the box. The background

scattering was estimated by measuring the intensity in pixels near the peak but not containing any peak tail. The choice of box size was made according to the width of each peak. Because of mosaic spread in the sample, the peaks were wider for higher orders. Consequently, the box was made wider for higher orders. The box size was chosen so that approximately 80% of the peak intensity was counted toward the integrated intensity.

### 3.2.4 Near Grazing Incidence Wide Angle X-ray Scattering Experiment

The high resolution wide angle X-ray scattering (WAXS) experiment was also carried out at the G1 station. The instrument was set up by the G1 station scientist, Arthur Woll, and the assistant scientist, Dr. Robin Baur. Wide angle X-ray scattering was collected at an incident angle of  $0.2^\circ$ . The total external reflection from an air-lipid interface occurs approximately at  $0.1^\circ$  and  $0.17^\circ$  for air-silicon interface, so  $0.2^\circ$  is not quite grazing incidence. Grazing incidence usually implies that the incident angle is less than the critical angle for a total external reflection. Therefore,  $0.2^\circ$  is called near grazing incidence (NGI) in this thesis. The background scattering was collected at  $-0.2^\circ$ . Subtraction of the negative angle data from the positive angle data resulted in a clean sample scattering image.

### 3.2.5 Transmission Wide Angle X-ray Scattering Experiment

The transmission wide angle X-ray scattering (TWAXS) experiment was also carried out at the G1 station. The incident angle  $\omega$  was set to  $-45^\circ$  for transmission data collection (see Fig. 3.13). A  $35\ \mu\text{m}$  thick silicon substrate absorbs 10.5 keV X-ray by only 20% [97], so most of the incoming X-rays penetrated the thin substrate.

Unfortunately, the axis of the rotation motor did not coincide with the sample axis, so the sample to detector distance varied as  $\omega$  was varied. To accurately measure the sample to detector distance, low angle scattering from a silver behenate (AgBe) sample was collected at a fixed  $\omega$ . Due to large mosaic spread of the AgBe sample, many orders were visible. While the relative intensity of each order was inaccurate, the positions of peaks were the same as those observed with a rotating sample. To measure the D-spacing of the sample,  $\omega$  was set to  $1^\circ$ . The sample to detector distance was measured to be 174.7 mm at  $\omega = 0^\circ$ . From the sample holder geometry shown in

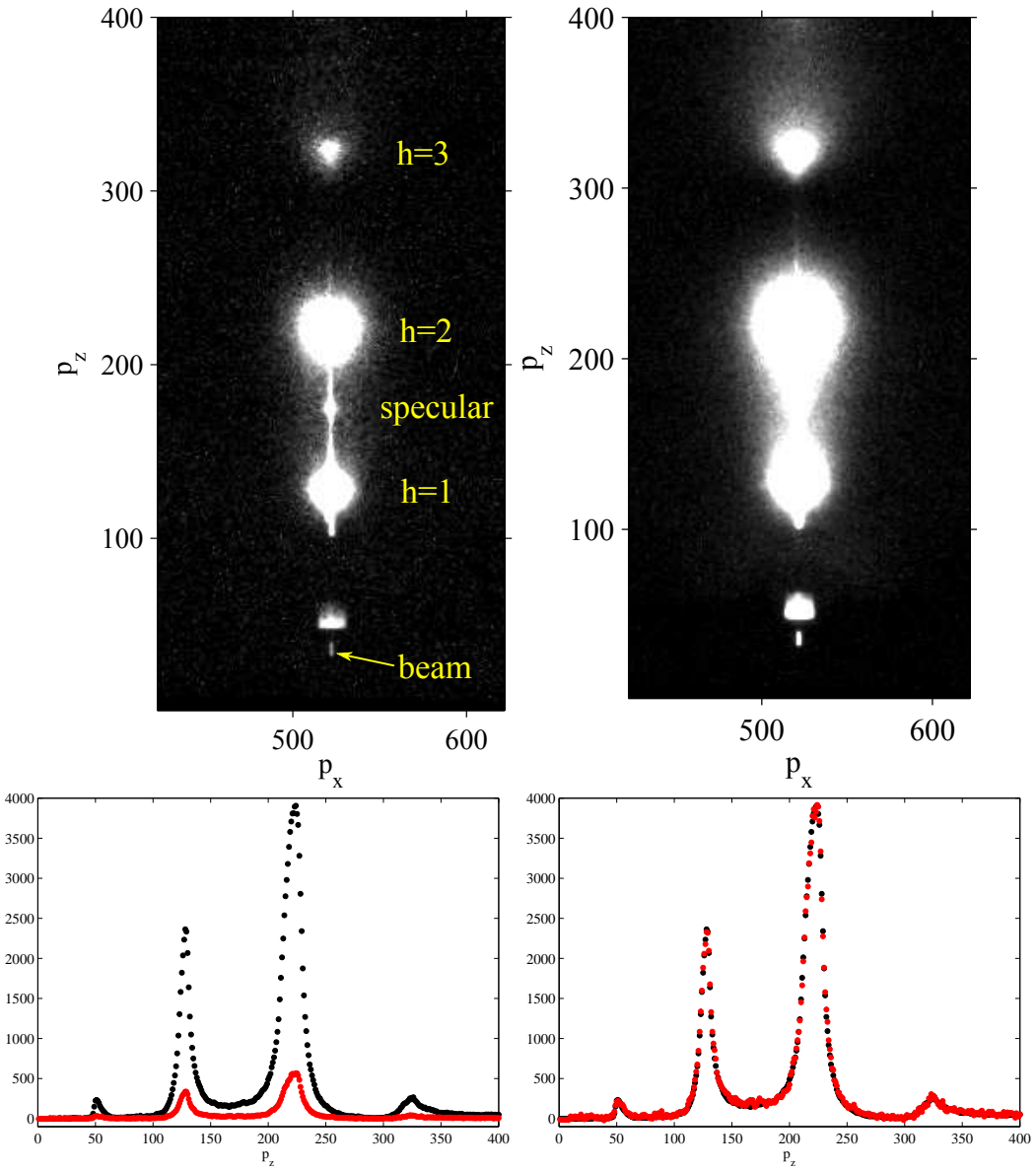


Figure 3.11: (top panels) CCD images of X-ray scattering taken with (left) and without (right) a nominally 25  $\mu\text{m}$  thick Mo attenuator. These data were taken at a fixed angle of incidence  $\omega = 0.8^\circ$ . The sample was an oriented film of DOPC:DOPE (3:1) in the fluid phase at 37 °C. The wavelength was 1.175 Å, the same as the one used for the ripple phase experiment. The same gray scale is used in both images. 100 pixel = 0.11  $\text{\AA}^{-1}$  in  $q$ . A small dot located about  $(p_x, p_z) = (520, 170)$  between the first and second orders is a specular reflection from the substrate. The exposure times were 1 second. (bottom panels) Vertical  $p_z$  slices of the X-ray images shown in the top panels (left). The scattering intensity measured with the attenuator (red solid circles) was multiplied by a factor of 6.9 and compared to the intensity measured without the attenuator (black solid circles, right).

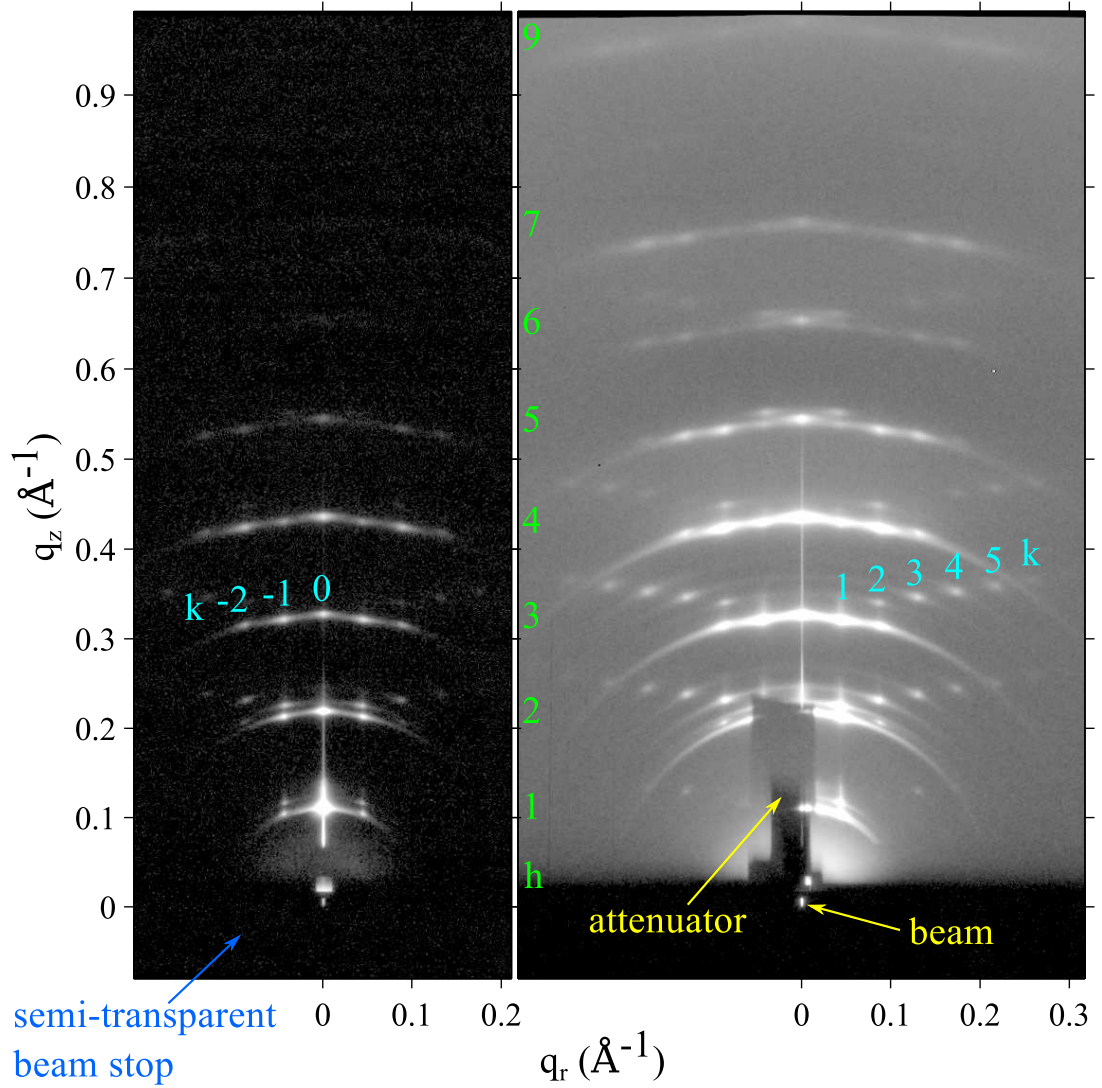


Figure 3.12: 1 second exposure (left) and 60 second exposure (right) of the low angle X-ray scattering from the DMPC ripple phase in gray log scales. The index  $h$  is labeled in green.  $(3, k)$  reflections are identified in cyan. The shadow cast by 100  $\mu\text{m}$  thick molybdenum attenuator blocking strong  $(1, 0)$  and  $(2, 0)$  orders in the right image is labeled as attenuator and extends from  $q_z = 0 \text{ \AA}^{-1}$  to  $0.2 \text{ \AA}^{-1}$ .  $D = 57.8 \text{ \AA}$ ,  $\lambda_r = 145.0 \text{ \AA}$ , and  $\gamma = 98.2^\circ$ .

Fig. 3.14, the sample to detector distance was estimated to be 158.6 mm at  $\omega = 45^\circ$ . A picture of the sample holder is shown in Fig. 3.15.

To level the sample, the sample was first leveled coarsely by watching the sample scattering. When  $\omega$  was negative, much of the incoming beam was absorbed by the flat substrate, yielding weak sample scattering. When  $\omega$  became positive, sample scattering was strong. With this procedure, we leveled the sample with an uncertainty of  $\pm 0.2^\circ$ . We then measured the beam intensity at various sample heights as a function of  $\omega$ . The sample was level when the beam intensity had the narrowest dip as the sample was moved vertically through the beam.

Background scattering was collected by replacing the sample with a bare wafer. The bare wafer was not placed exactly at the same location as the sample, which gave slightly different background scattering. This only affected the background subtraction near the beam. The wide angle scattering was not affected by this inexact placement of the bare wafer.

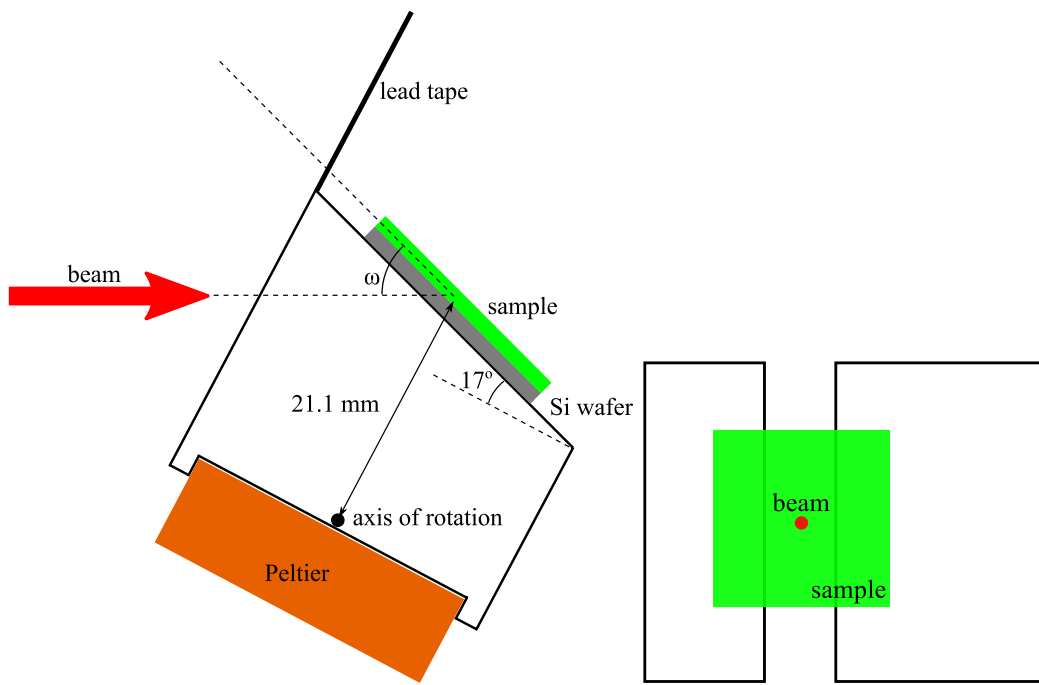


Figure 3.13: Schematics of the sample holder in the transmission mode. Side (left) and top (right) views are shown. The thickness of the Si wafer =  $35 \mu\text{m}$ . The thickness of the sample  $\approx 10 \mu\text{m}$ . The distance between the axis of rotation and sample = 21.1 mm.

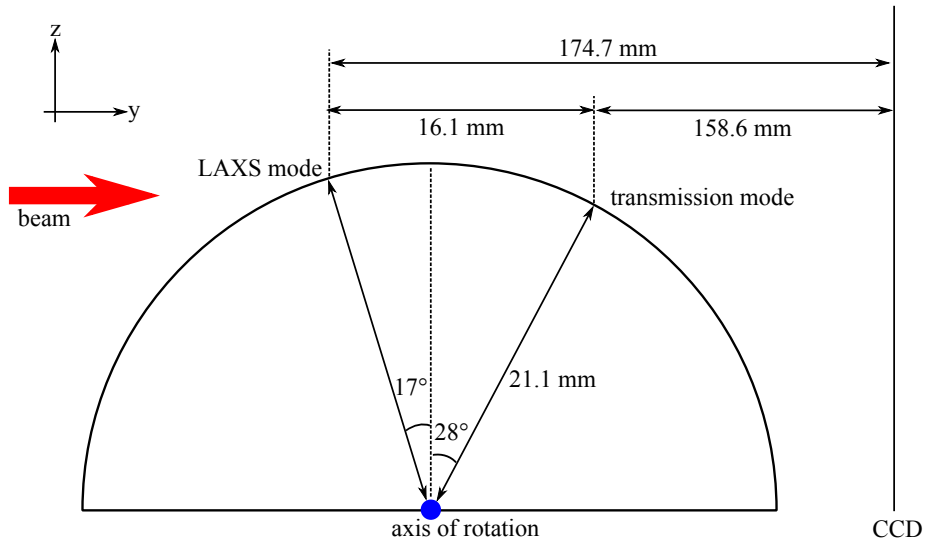


Figure 3.14: Circular path followed by the sample as the angle of incidence  $\omega$  was changed. The sample to detector distance and  $D$ -spacing of the sample were measured in the LAXS mode, where  $\omega = 1^\circ$ . WAXS images were collected at the transmission mode, where  $\omega = -45^\circ$ . The  $z$  position of the sample was slightly higher at the LAXS mode than at the transmission mode, so the sample holder was vertically shifted for different modes.

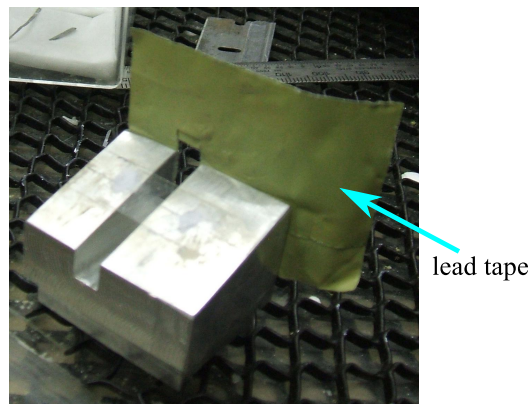


Figure 3.15: Picture of the sample holder looking from above. A lead tape was attached to the back of the sample holder to help reduce the background scattering, typically coming from the air gap between the flightpath snout and the mylar window of the chamber.

### 3.3 LAXS: analysis

#### 3.3.1 Lattice Structure

The unit cell vectors for the two-dimensional oblique lattice shown in Fig. 3.1 can be expressed as

$$\mathbf{a} = \frac{D}{\tan \gamma} \hat{\mathbf{x}} + D \hat{\mathbf{z}} \quad (3.3)$$

and

$$\mathbf{b} = \lambda_r \hat{\mathbf{x}}. \quad (3.4)$$

The corresponding reciprocal lattice unit cell vectors are

$$\mathbf{A} = \frac{2\pi}{D} \hat{\mathbf{z}} \quad (3.5)$$

and

$$\mathbf{B} = \frac{2\pi}{\lambda_r} \hat{\mathbf{x}} - \frac{2\pi}{\lambda_r \tan \gamma} \hat{\mathbf{z}}. \quad (3.6)$$

The reciprocal lattice vector,  $\mathbf{q}_{hk}$  for the Bragg peak with Miller indices  $(h, k)$  is

$$\mathbf{q}_{hk} = h\mathbf{A} + k\mathbf{B}, \quad (3.7)$$

so its Cartesian components are

$$\mathbf{q}_{hk} \cdot \hat{\mathbf{x}} = q_{hk}^x = \frac{2\pi k}{\lambda_r} \equiv q_k^x \quad (3.8)$$

$$\mathbf{q}_{hk} \cdot \hat{\mathbf{y}} = q_{hk}^y = 0 \quad (3.9)$$

$$\mathbf{q}_{hk} \cdot \hat{\mathbf{z}} = q_{hk}^z = \frac{2\pi h}{D} - \frac{2\pi k}{\lambda_r \tan \gamma}. \quad (3.10)$$

Our sample consists of many ripple domains with a uniform distribution of in-plane directions of the ripple wave vector,  $\mathbf{b}$  in Fig. 3.1. In this case,  $q_{hk}^x$  and  $q_{hk}^y$  are combined to give  $q_{hk}^r = 2\pi k / \lambda_r$ .

### 3.3.2 Sample q-space

The incoming and outgoing wavevectors of the x-ray beam in Fig. 3.16 are given by

$$\mathbf{k}_{\text{in}} = \frac{2\pi}{\lambda} \hat{\mathbf{y}}, \quad \mathbf{k}_{\text{out}} = \frac{2\pi}{\lambda} (\sin 2\theta \cos \phi \hat{\mathbf{x}} + \cos 2\theta \hat{\mathbf{y}} + \sin 2\theta \sin \phi \hat{\mathbf{z}}), \quad (3.11)$$

where  $\lambda$  is the wavelength of x-ray,  $2\theta$  is the total scattering angle, and  $\phi$  is the angle measured from the equator on the detector. The scattering vector (also called momentum transfer vector) is the difference between  $\mathbf{k}_{\text{in}}$  and  $\mathbf{k}_{\text{out}}$ ,

$$\begin{aligned} \mathbf{q} &= \mathbf{k}_{\text{out}} - \mathbf{k}_{\text{in}} \\ &= q (\cos \theta \cos \phi \hat{\mathbf{x}} - \sin \theta \hat{\mathbf{y}} + \cos \theta \sin \phi \hat{\mathbf{z}}), \end{aligned} \quad (3.12)$$

where  $q = 4\pi \sin \theta / \lambda$  is the magnitude of the scattering vector. When the sample is rotated by  $\omega$  about the lab x-axis in the clockwise direction as shown in Fig. 3.16, the sample  $q$ -space also rotates and are given by

$$\hat{\mathbf{e}}_x = \hat{\mathbf{x}}, \quad \hat{\mathbf{e}}_y = \cos \omega \hat{\mathbf{y}} + \sin \omega \hat{\mathbf{z}}, \quad \hat{\mathbf{e}}_z = -\sin \omega \hat{\mathbf{y}} + \cos \omega \hat{\mathbf{z}}. \quad (3.13)$$

From Eq. (3.12) and (3.13), we find Cartesian components of the sample  $q$ -space to be

$$\begin{aligned} q_x &= \mathbf{q} \cdot \hat{\mathbf{e}}_x = q \cos \theta \cos \phi, \\ q_y &= \mathbf{q} \cdot \hat{\mathbf{e}}_y = q (-\sin \theta \cos \omega + \cos \theta \sin \phi \sin \omega), \\ q_z &= \mathbf{q} \cdot \hat{\mathbf{e}}_z = q (\sin \theta \sin \omega + \cos \theta \sin \phi \cos \omega). \end{aligned} \quad (3.14)$$

The position,  $(X, Z)$ , of a CCD pixel is measured with respect to the beam and given by

$$X = S \tan 2\theta \cos \phi, \quad Z = S \tan 2\theta \sin \phi, \quad (3.15)$$

where  $S$  is the distance between the sample and detector.

From a model for the electron density of a lipid bilayer, one calculates the X-ray scattering intensity pattern,  $I(\mathbf{q})$ . Then, Eq. (3.14) and (3.15) relate  $I(\mathbf{q})$  to the experimentally measured intensity pattern,  $I(X, Z)$ . It is important to remember that a given pixel position,  $(X, Z)$ , corresponds to a triplet  $(q_x, q_y, q_z)$ . Fully exploring the sample  $q$ -space requires changing  $\omega$  for a fixed wavelength, which was achieved

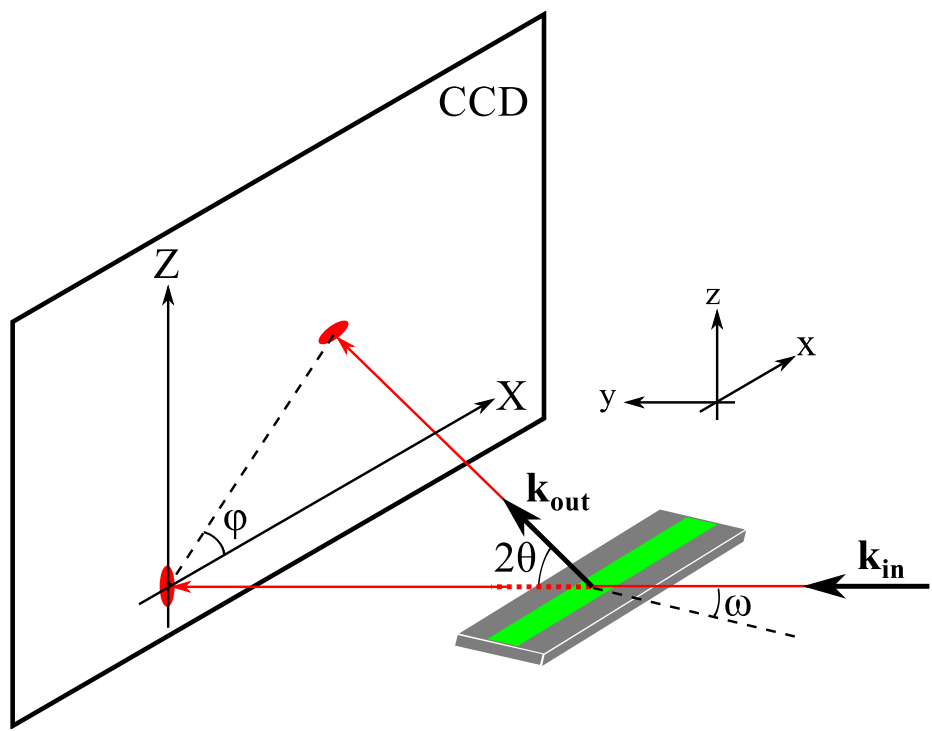


Figure 3.16: Experimental reflectivity geometry.

by continuously rotating the sample with a motor. In the ripple phase, because our sample has in-plane rotational symmetry, the ripple side peaks ( $h, k \neq 0$ ) make up Bragg rings while the main peaks ( $h, k = 0$ ) are still delta function like (see Fig. 3.17) in  $q$ -space. In order for the main peak to be observed,  $\omega$  must be equal to  $\theta_B$ , but the side peaks are observed at any  $\omega$ . Those side peaks get slightly smeared due to integration over  $q_y$ .

For low angle x-ray scattering (LAXS), it is convenient to linearize the above equations in terms of  $\theta$  and  $\omega$ . In the small angle approximation,  $\sin \phi \approx Z/(2S\theta)$  and  $\cos \phi \approx X/(2S\theta)$ , and

$$\begin{aligned} q_x &\approx \frac{4\pi\theta \cos \phi}{\lambda} \approx kX/S \\ q_y &\approx q_z \omega - \frac{4\pi\theta^2}{\lambda} \approx q_z \omega - \frac{\lambda q_z^2}{4\pi} \\ q_z &\approx \frac{4\pi\theta \sin \phi}{\lambda} \approx kZ/S, \end{aligned} \quad (3.16)$$

with  $k = 2\pi/\lambda$ . For wide angle X-ray scattering, the exact relations given by Eq. (3.14) are necessary. Especially in the transmission experiment, where  $\omega$  is large, an observed X-ray pattern appears nontrivial and becomes almost impossible to analyze without the use of Eq. (3.14). The transmission experiment is discussed in Sec.3.7.

### 3.3.3 Lorentz Correction

Our sample has in-plane rotational symmetry about the  $z$ -axis. Ignoring mosaic spread to which we will come back later, this means that the sample consists of many domains with differing ripple directions, all domains being parallel to the substrate. In sample  $q$ -space, ripple ( $h, k \neq 0$ ) side peaks are represented as rings centered at the meridian, or  $q_z$ -axis, while ( $h, k = 0$ ) main peaks are still points on the meridian (see Fig. 3.17). Then, for an arbitrary incident angle  $\omega$ , ( $h, 0$ ) peaks are not observed while side peaks are observed for a range of  $\omega$  as will now be explained.

In order to capture all ( $h, k$ ) peaks in one X-ray exposure, the sample was continuously rotated over a range of  $\omega, \Delta\omega$ , about the  $x$ -axis. As a result of this rotation, the ( $h, 0$ ) main peaks become arcs that subtend an angle  $\Delta\omega$ , as shown in Fig. 3.18, with its length equal to  $\Delta\omega q_{h0}$ . The detector records the intersections of these arcs

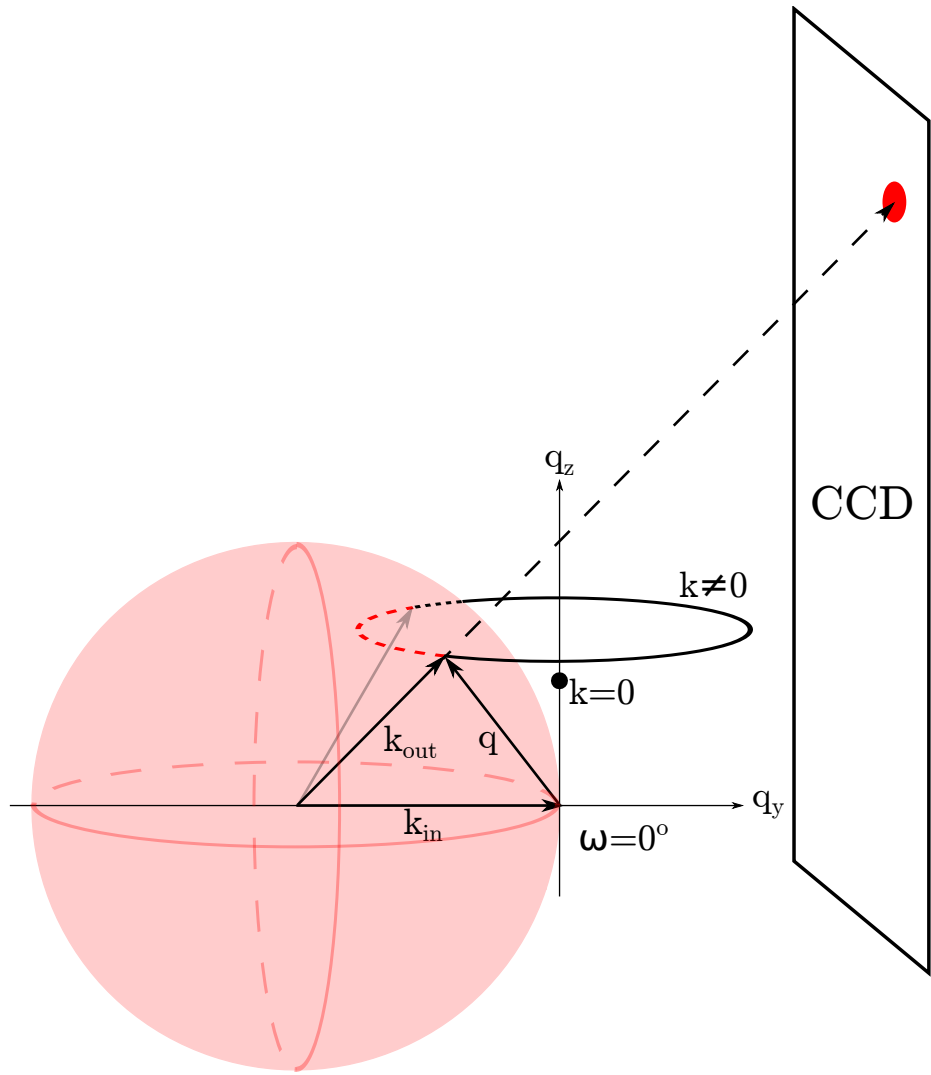


Figure 3.17: Ewald sphere construction for the ripple phase diffraction in the low angle regime. A ripple  $k = 0$  peak is the solid, black circle on the  $q_z$ -axis. A ripple  $k \neq 0$  ring is the black ring centered about the  $q_z$ -axis. The portion of the ring that is inside the Ewald sphere is shown as a red dashed line and the portion of the ring that is outside but behind the Ewald sphere is shown as a black dotted line. The magnitude of the total scattering angle is exaggerated. With a wavelength of  $1.175 \text{ \AA}$ , the magnitude  $|k_{in}| = 5.35 \text{ \AA}^{-1}$ . For a  $h = 5$  peak,  $q_{50}^z = 0.54 \text{ \AA}^{-1}$ , one tenth of  $k_{in}$ .

with the Ewald sphere, so the intrinsic scattering intensity of the  $(h, k = 0)$  reflections is the product of the observed intensity,  $I_{hk}^{\text{obs}}$  with the arc length, that is,

$$I_{h0} = \Delta\omega q_{h0}^z I_{h0}^{\text{obs}}. \quad (3.17)$$

This is the usual Lorentz correction for lamellar orders.

Now, we consider relative intensity of side peaks for a given order  $h$ . As described earlier,  $(h, k \neq 0)$  side peaks are represented as rings whose radius is  $q_{hk}^r$  in the sample  $q$ -space. Because only the domains with the right ripple direction can satisfy the Bragg's condition at a given fixed angle  $\omega$ , the intrinsic scattering intensity in this ring is reduced by a factor of  $2\pi q_k^r$  compared to the  $(h, 0)$  reflections. This reduction of intensity can be nicely visualized by the Ewald sphere construction shown in Fig. 3.17, which shows that the entire rings are not intersected by the Ewald sphere at a fixed angle. Then, the intrinsic scattering intensity in a ring is

$$I_{hk \neq 0} \propto 2\pi q_{hk}^r I_{hk}^{\text{obs}}. \quad (3.18)$$

During an X-ray exposure, the sample  $q$ -space rotates and the rings are intersected by the Ewald sphere at all our experimental incident angles  $\omega$ . However, as Fig. 3.19 shows, only small parts of the rings are actually intersected with the Ewald sphere. To obtain the full expression for  $(h, k \neq 0)$  reflections, we now turn to a more rigorous calculation.

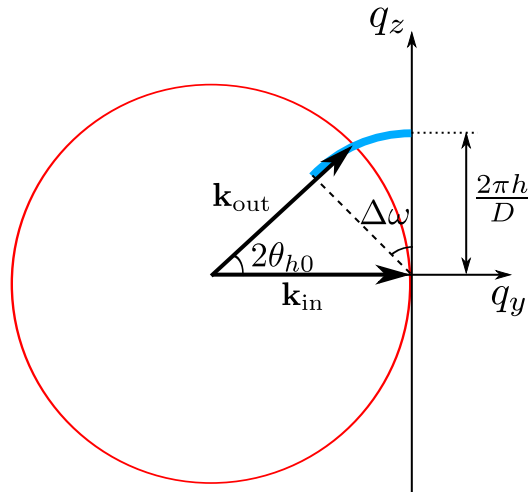


Figure 3.18: Side view of an arc of  $k = 0$  peak shown as a thick blue line.

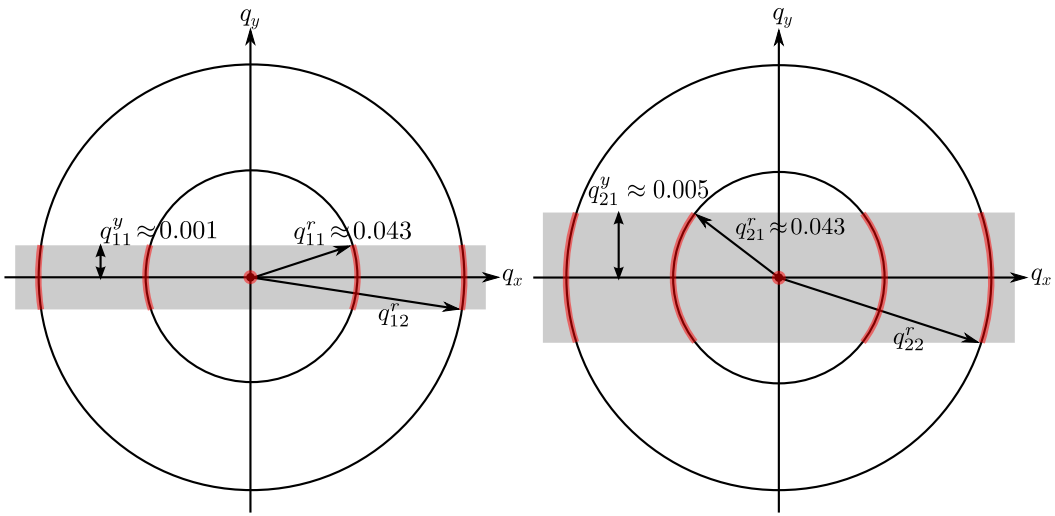


Figure 3.19:  $q$ -space representations of Bragg peaks and Bragg rings for  $h = 1$  and  $2$  and  $k = 0, 1$ , and  $2$  in  $q_{hk}^z$  planes. The intersection between the Ewald sphere and a Bragg peak/ring is indicated in red. The observed intensity for the  $k \neq 0$  orders is proportional to the fraction of the length of red arcs in the circumference. This fraction is equal to one for  $k = 0$  reflections. Because the reflections are not in the same  $q_z$  plane, the range of  $q_y$  integration indicated by the height of the gray rectangle is different for different  $h$  orders. For  $\gamma \neq 90^\circ$ , the range of  $q_y$  integration is slightly different for different  $k$  reflections with the same  $h$ . The values shown are for  $D = 58$  Å,  $\lambda_r = 145$  Å,  $\gamma = 90^\circ$ , and  $\lambda = 1.175$  Å. The magnitude of curvature of arcs is exaggerated.

Mathematically, the rotation is equivalent to an integration over  $\omega$ . In low angle X-ray scattering,  $q_z$  is nearly constant at a given pixel as  $\omega$  is changed, which can be seen from Eq. (3.16). As Eq. (3.16) shows,  $\omega$  dependence appears only through  $q_y$ , so rotating the sample is realized by integrating over  $q_y$ ; formally, we write  $d\omega = dq_y/q_z$ . To derive the integration limits on  $q_y$ , let us consider two cases: (1) When  $\omega \leq 0$ , the incoming X-ray beam is blocked by the back of the substrate. This sets the lower limit of  $\omega$  to 0. Plugging  $\omega = 0$  in Eq. 3.16), we find the lower limit of the  $q_y$  integration to be  $-\lambda q_z^2/(4\pi)$ . (2) When  $\omega \geq 2\theta$ , the substrate blocks the outgoing X-ray, so the maximum  $\omega = 2\theta$ . Within the small angle approximation,  $q_z \approx 4\pi\theta/\lambda$ . Then, the maximum  $\omega$  can be expressed as  $\lambda q_z/(2\pi)$ . Plugging this expression for  $\omega$  in Eq. (3.16), we find the upper limit of the  $q_y$  integration to be  $\lambda q_z^2/(4\pi)$ . Also integrating over the detector pixels  $X$  and  $Z$  to obtain integrated intensity, we write the observed intensity as

$$\begin{aligned} I_{hk}^{\text{obs}} &\propto \int dX \int dZ \int d\omega I_{hk} \\ &\propto \int dq_x \int dq_z \int_{-\frac{\lambda q_z^2}{4\pi}}^{\frac{\lambda q_z^2}{4\pi}} \frac{dq_y}{q_z} I_{hk}(\mathbf{q}), \end{aligned} \quad (3.19)$$

where  $1/q_z$  factor in  $q_y$  integration is the usual Lorentz polarization factor in the small angle approximation.

For a crystalline sample with in-plane rotational symmetry, the structure factor of a ripple Bragg peak is

$$S_{hk}(\mathbf{q}) = S_{hk}(q_r, q_z) = \frac{1}{2\pi q_r} \delta(q_r - q_{hk}^r) \delta(q_z - q_{hk}^z), \quad (3.20)$$

where  $q_{hk}^r = 2\pi|k|/\lambda_r$ . Thus, the scattering pattern in the ripple phase is a collection of Bragg rings for  $k \neq 0$  centered at the meridian and the Bragg peaks for  $k = 0$  located along the meridian. The scattering intensity is  $I(\mathbf{q}) = |F(\mathbf{q})|^2 S(\mathbf{q})$ , where  $F(\mathbf{q})$  is the form factor. After the  $q_z$  integration, the observed, integrated intensity of  $(h, k)$  peak is proportional to

$$I_{hk}^{\text{obs}} \propto \frac{|F_{hk}|^2}{q_{hk}^z} \int dq_x \int_{-q_{hk}^{y0}}^{q_{hk}^{y0}} dq_y \frac{\delta(q_r - q_{hk}^r)}{2\pi q_r}, \quad (3.21)$$

where  $q_{hk}^{y0} = \lambda(q_{hk}^z)^2/(4\pi)$ . For side peaks ( $k \neq 0$ ), we have

$$\begin{aligned} \int dq_x \int_{-q_{hk}^{y0}}^{q_{hk}^{y0}} dq_y \frac{\delta(q_r - q_{hk}^r)}{2\pi q_r} &\approx \int_{-q_{hk}^{y0}/q_{hk}^r}^{q_{hk}^{y0}/q_{hk}^r} d\phi \int dq_r q_r \frac{\delta(q_r - q_{hk}^r)}{2\pi q_r} \\ &= \frac{q_{hk}^{y0}}{\pi q_{hk}^r}. \end{aligned} \quad (3.22)$$

For main peaks ( $k = 0$ ), we have

$$\begin{aligned} \int dq_x \int_{-q_{hk}^{y0}}^{q_{hk}^{y0}} dq_y \frac{\delta(q_r - q_{hk}^r)}{2\pi q_r} &= \int_0^{2\pi} d\phi \int dq_r q_r \frac{\delta(q_r - q_{hk}^r)}{2\pi q_r} \\ &= 1 \end{aligned} \quad (3.23)$$

Using Eq. (3.21 – 3.23), we write the observed integrated intensity as

$$I_{h0}^{\text{obs}} \propto \frac{|F_{h0}|^2}{q_{h0}^z} \quad (3.24)$$

$$I_{hk}^{\text{obs}} \propto \frac{|F_{hk}|^2}{q_{hk}^z} \frac{q_{hk}^{y0}}{\pi q_{hk}^r} = |F_{hk}|^2 \frac{\lambda q_{hk}^z}{2\pi} \frac{1}{2\pi q_{hk}^r} = |F_{hk}|^2 \frac{2\theta_{hk}}{2\pi q_{hk}^r}, \quad (3.25)$$

where  $2\theta_{hk} = \lambda q_{hk}^z/(2\pi)$  is the incident angle at which the outgoing X-ray for the peak  $(h, k)$  is blocked by the substrate. Eq. (3.24) and (3.25) relate the form factor calculated from a model to the experimentally observed intensity, and are partially equivalent to Eq. (3.17) and (3.18).

In non-linear least squares fitting procedure, we fitted the observed integrated intensity to the calculated intensity from a bilayer model using these Lorentz corrections. This is because we can determine experimental uncertainties on observed intensity rather than the Lorentz-corrected form factors. We avoid propagating the uncertainties by fitting a model to observed intensity.

### 3.3.4 Absorption Correction for LAXS

In this section, we derive the absorption correction for an oriented sample. The calculation involves an explicit integration over the incident angle,  $\omega$ , which is necessitated by the sample rotation during an X-ray exposure. The procedure is to write down an absorption factor,  $A(\omega, \theta)$ , for a given scattering angle at a given incident angle,

and then integrate over  $\omega$ . We ignore  $q_x$  dependence because the X-ray path inside the sample is nearly within the  $y$ - $z$  plane for low angle scattering. The correction for wide angle scattering is described in a later section.

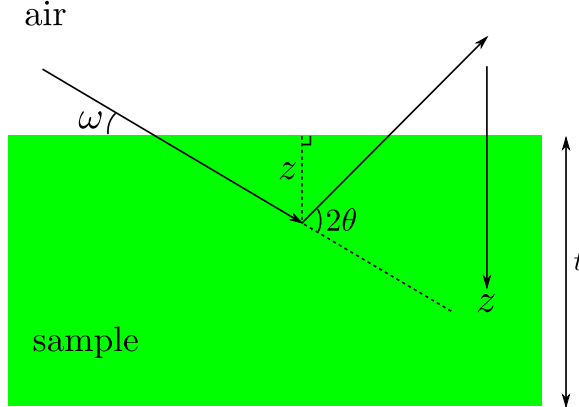


Figure 3.20: The path of X-rays within the sample. The incident angle is  $\omega$  and the total scattering angle is  $2\theta$ . An X-ray with a penetration depth of  $z$  is shown. The total thickness of the sample is  $t$ . Refraction correction is smaller than what? for  $\theta > 0.5^\circ$  ( $h = 1$ ).

Assume that all the X-rays enter the sample from the top surface. The total scattering angle is given by  $2\theta$  (see Fig. 3.20). Let the  $z$ -axis point downward. At the top surface (air-sample interface),  $z = 0$ . For X-rays that travel to  $z$  and then scatter, the total path length within the sample is

$$L(z, \omega, \theta) = \frac{z}{\sin \omega} + \frac{z}{\sin(2\theta - \omega)} = z g(\omega, \theta), \quad (3.26)$$

where  $g(\omega, \theta) = (\sin \omega)^{-1} + (\sin(2\theta - \omega))^{-1}$ . For each ray, the intensity is attenuated by the sample absorption. If non-attenuated intensity is equal to  $I_0$ , then the attenuated intensity is

$$I(z, \omega, \theta) = I_0 \exp\left(-\frac{L}{\mu}\right), \quad (3.27)$$

where  $\mu$  is the absorption length of an X-ray.  $\mu$  is about 2.6 mm for 10.5 keV for both water and lipids in all phases [97]. The observed intensity of scattering from a sample fixed at an angle  $\omega$  is equal to the integration of Eq. (3.27) over the total

thickness of the sample and given by

$$\begin{aligned} I(\omega, \theta) &= \int_0^t dz I(z, \omega, \theta) = I_0 \int_0^t dz \exp\left(-\frac{g(\omega, \theta)}{\mu} z\right) \\ &= I_0 \mu \frac{1 - \exp\left(-\frac{t}{\mu} g(\omega, \theta)\right)}{g(\omega, \theta)}. \end{aligned} \quad (3.28)$$

Defining the absorption factor at a fixed angle to be  $A(\omega, \theta)$ , the observed intensity can also be written as

$$I(\omega, \theta) = A(\omega, \theta) t I_0, \quad (3.29)$$

where  $t I_0$  is the intensity we would observe for non-absorbed X-rays. Equating Eq. (3.28) and (3.29), we get

$$A(\omega, \theta) = \frac{\mu}{t} \frac{1 - \exp\left(-\frac{t}{\mu} g(\omega, \theta)\right)}{g(\omega, \theta)}. \quad (3.30)$$

If  $\mu$  is taken to infinity (no absorption),  $A(\omega, \theta)$  goes to 1 as expected. The absorption factor  $A_{h0}$  for the  $k = 0$  peaks is given by  $A(\omega = \theta = \theta_B)$ , plotted in Fig. 3.21. As shown, this factor is about 20 % for  $h = 1$  peak relative to  $h = 4$ , so it is not negligible.

For  $k \neq 0$  side peaks, an integration over the incident angle  $\omega$  is necessary because these peaks are observable at all our experimental incident angles as described in section 3.3.3. The observed intensity for side peaks from a rotating sample is simply

$$I_{\text{obs}}(\theta) = \int_0^{2\theta} d\omega I(\omega, \theta). \quad (3.31)$$

The upper integration limit is equal to  $2\theta$  because the substrate completely blocks the scattered X-rays above this angle as discussed in section 3.3.3. Eq. (3.30), which is essentially the integrand in Eq. (3.31), is plotted in Fig. 3.22. It is maximum when  $\omega = \theta$ , meaning that the path length is shortest at the Bragg condition. The non-attenuated observed intensity is equal to  $2\theta t I_0$ . We, then, define the absorption factor  $A(\theta)$  to be the ratio of the total observed intensity to the total non-attenuated intensity,

$$A(\theta) \equiv \frac{I_{\text{obs}}(\theta)}{2\theta t I_0}. \quad (3.32)$$

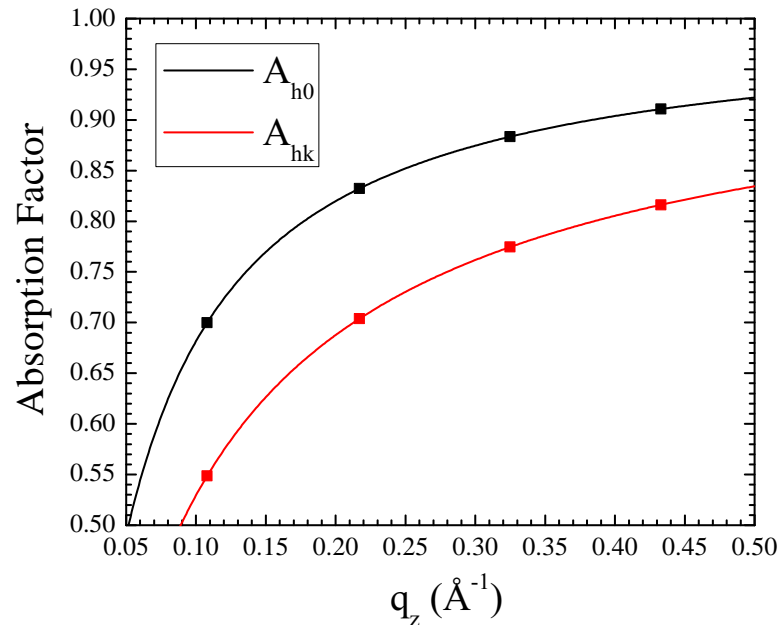


Figure 3.21: Absorption factors as a function of  $q_z \approx 4\pi\theta/\lambda$ . Values at  $q_z = 2\pi h/D$  corresponding to  $D = 57.8 \text{ \AA}$  are shown as squares.  $\mu = 2600 \mu\text{m}$ ,  $t = 10 \mu\text{m}$ , and  $\lambda = 1.175 \text{ \AA}$ .

Using Eq. (3.30) and (3.31) in (3.32), we arrive at the final absorption factor

$$A(\theta) = \frac{1}{2\theta} \int_0^{2\theta} d\omega A(\omega, \theta) = \frac{\mu}{2\theta t} \int_0^{2\theta} d\omega \frac{1 - \exp\left(-\frac{t}{\mu}g(\omega, \theta)\right)}{g(\omega, \theta)}. \quad (3.33)$$

$A_{hk} = A(\theta)$  is plotted in Fig. 3.21. The absorption correction  $A_c(\theta)$  is the inverse of Eq. (3.33).

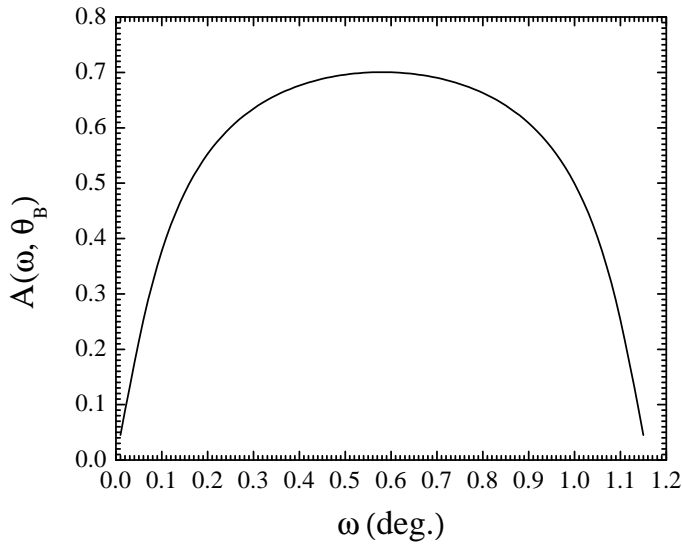


Figure 3.22: Eq. (3.30) plotted as a function of  $\omega$  for  $\theta = \theta_B = 0.58^\circ$ , corresponding to a Bragg angle for  $D = 57.8 \text{ \AA}$ .

### 3.3.5 Correction due to mosaic spread

Integrated intensity needs to be corrected for mosaic spread. During an X-ray exposure, the sample was continuously rotated. Due to this rotation, each pixel integrates intensity over a range of incident angles  $\omega$ . As described in appendix A.2.2, a mosaic spread distribution can be probed by changing  $\omega$ , so rotating the sample is essentially equivalent to integrating a mosaic spread distribution. Because the range of the distribution probed is approximately given by  $\omega = [0, 2\theta_{hk}]$  where  $\theta_{hk}$  is the Bragg angle for a  $(h, k)$  reflection, this range is larger for higher  $h$  orders. This effect is illustrated in Fig. 3.23.

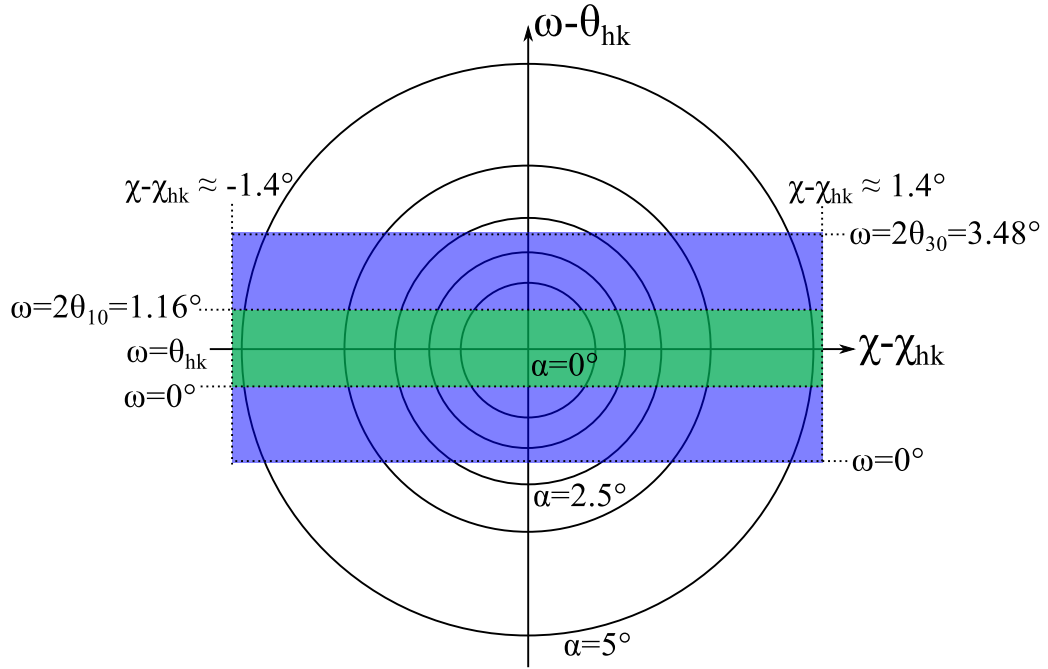


Figure 3.23: Contours of a mosaic spread distribution projected on the  $\omega\chi$ -plane, where  $\chi - \chi_{hk}$  is an angle measured from a  $(h, k)$  reflection on the detector ( $\chi = \pi/2 - \phi$  in Fig. 3.16) and  $\theta_{hk}$  is the Bragg angle for a  $(h, k)$  reflection. The distribution function takes a form of Lorentzian centered at  $\alpha = 0$ . Domains with  $\alpha = 0$  are probed at  $\omega = \theta_{hk}$  and  $\chi = \chi_{hk}$ . Integrated intensity of  $(1, k)$  reflection arises from domains in the green shaded area while that of  $(3, k)$  reflection is from the blue shaded area, which is three times larger.

We limit  $\chi - \chi_{hk}$  to go from  $-1.4^\circ$  to  $1.4^\circ$ . The effect of cutoff on  $\chi - \chi_{hk}$  is not very important because most of observed intensity was included in integration boxes. In contrast, cutoff on  $\omega$  due to substrate blocking the scattering is important, especially for lower  $h$  orders.

We take the distribution to be Lorentzian, which has been experimentally observed (REF, Dr. Nagle),

$$P(\alpha) = \frac{N}{\alpha^2 + \alpha_M^2}, \quad (3.34)$$

where  $N$  is a normalization constant and  $\alpha_M$  is the HWHM of the distribution.  $N$  satisfies

$$N \approx \frac{1}{2\pi} \left( \int_0^{\frac{\pi}{2}} d\alpha \frac{\alpha}{\alpha^2 + \alpha_M^2} \right)^{-1}. \quad (3.35)$$

We then consider a two dimensional contour map on a  $\omega\chi$  plane. Intensity for a reflection with a Bragg angle of  $\theta_B$  is given by

$$I = \int_{-\theta_B}^{\theta_B} d\omega \int_{-\chi_0}^{\chi_0} d\chi P(\alpha) = \int_{-\theta_B}^{\theta_B} d\omega \int_{-\chi_0}^{\chi_0} d\chi \frac{N}{\omega^2 + \chi^2 + \alpha_M^2} \quad (3.36)$$

After the integration over  $\chi$ , Eq. (3.36) is

$$I = 4N \int_0^{\theta_B} \frac{d\omega}{\sqrt{\omega^2 + \alpha_M^2}} \arctan\left(\frac{\chi_0}{\sqrt{\omega^2 + \alpha_M^2}}\right). \quad (3.37)$$

Eq. (3.37) is plotted in Fig. 3.24.

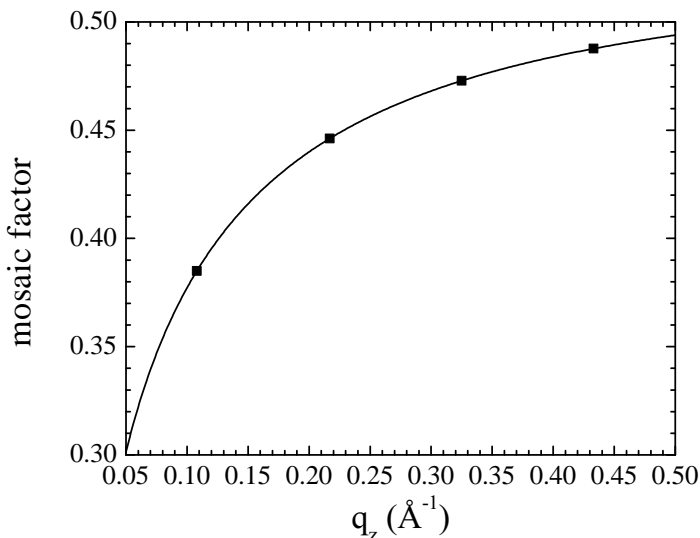


Figure 3.24: Mosaic factor given by Eq. (3.37) as a function of  $q_z \approx 4\pi\theta/\lambda$ . Values at  $q_z = 2\pi h/D$  corresponding to  $D = 57.8 \text{ \AA}$  are shown as squares.  $\alpha_M = 0.05^\circ$  and  $\chi_0 = 1.4^\circ$ . Eq. (3.37) reaches  $\sim 0.54$  at  $\theta_B = \pi/2$  and  $\chi_0 = 1.4^\circ$  and reaches  $\sim 1$  at  $\theta_B = \pi/2$  and  $\chi_0 = 1.4^\circ$  as expected.

## 3.4 LAXS: model

### 3.4.1 Contour Part of the Form Factor

As in Ref. [87], we take the ripple profile to have a sawtooth profile. Its amplitude is  $A$  and the projection of the major arm on the ripple direction is  $x_M$  as shown in Fig. 3.1. Then, we write the ripple profile as

$$u(x) = \begin{cases} -\frac{A}{\lambda_r - x_0} \left( x + \frac{\lambda_r}{2} \right) & \text{for } -\frac{\lambda_r}{2} \leq x < -\frac{x_0}{2}, \\ \frac{A}{x_0} x & \text{for } -\frac{x_0}{2} \leq x \leq \frac{x_0}{2}, \\ -\frac{A}{\lambda_r - x_0} \left( x - \frac{\lambda_r}{2} \right) & \text{for } \frac{x_0}{2} < x \leq \frac{\lambda_r}{2}. \end{cases} \quad (3.38)$$

The ripple profile has inversion symmetry, so that the resulting form factor is real.  $A$  and  $x_M$  are fitting parameters that depend on the integrated intensity of each peak while  $D$ ,  $\lambda_r$ , and  $\gamma$  are determined from measuring the positions of the Bragg peaks.

In order to allow the electron density along the ripple direction to modulate, we include two additional parameters, one to allow for the electron density across the minor side to be different by a ratio  $f_1$  from the electron density across the major side and a second parameter  $f_2$ , which is multiplied by  $\delta$  functions  $\delta(x \pm x_M/2)$  to allow for a different electron density near the kink between the major and the minor sides.

The contour part of the form factor  $F_C$  calculated from Eq. (3.38) is plotted in Fig. (3.25).

### 3.4.2 Transbilayer Part of the Form Factor

#### 1G and 2G hybrid model

In the hybrid model, the terminal methyl region of the bilayer is represented as a Gaussian function [98]. The headgroups are represented by one and two Gaussian functions in 1G and 2G hybrid model, respectively. The methylene and water regions are each treated as a constant. The gap between the two constants is represented by a sine function. Then, for half of the bilayer,  $0 \leq z \leq D/2$ , the electron density has the form,

$$\rho(z) = \rho_G(z) + \rho_S(z) + \rho_B(z), \quad (3.39)$$

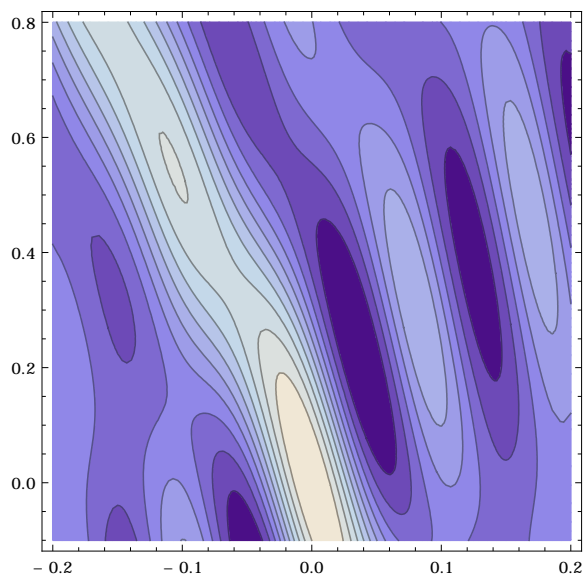


Figure 3.25: Not sure if this plot is useful. The horizontal axis is  $q_x$  and the vertical axis is  $q_z$ .

where the Gaussian part is given by

$$\rho_G(z) = \sum_{i=1}^{1 \text{ or } 2} \rho_{Hi} e^{-(z-Z_{Hi})^2/(2\sigma_{Hi}^2)} + \rho_M e^{-z^2/(2\sigma_M^2)}, \quad (3.40)$$

the strip part is given by

$$\rho_S(z) = \begin{cases} \rho_{CH_2} & \text{for } 0 \leq z < Z_{CH_2}, \\ \rho_W & \text{for } Z_W \leq z \leq D/2, \end{cases} \quad (3.41)$$

and the bridging part is given by

$$\rho_B(z) = \frac{\rho_W - \rho_{CH_2}}{2} \cos \left[ \frac{-\pi}{\Delta Z_H} (z - Z_W) \right] + \frac{\rho_W + \rho_{CH_2}}{2} \quad \text{for } Z_{CH_2} < z < Z_W. \quad (3.42)$$

with  $\Delta Z_H = Z_W - Z_{CH_2}$ . Here, we assume  $Z_{H2} > Z_{H1}$ . Table 3.5 shows some of the definitions.

	1G	2G
$Z_{CH_2}$	$Z_{H1} - \sigma_{H1}$	$Z_{H1} - \sigma_{H1}$
$Z_W$	$Z_{H1} + \sigma_{H1}$	$Z_{H2} + \sigma_{H2}$

Table 3.5: Definitions of  $Z_{CH_2}$  and  $Z_W$

The transbilayer profile along  $x = -z \tan \psi$  can be obtained by rotating the coordinates  $x$  and  $z$  by  $\psi$  in the clockwise direction and reexpressing  $\rho(z)$  in terms of the rotated coordinates. This leads to replacing  $x$  with  $x' = x \cos \psi + z \sin \psi$  and  $z$  with  $z' = -x \sin \psi + z \cos \psi$ . Then, the rotated transbilayer profile is

$$\rho(x, z) = \delta(x + z \tan \psi) [\rho_G(z') + \rho_S(z') + \rho_B(z')]. \quad (3.43)$$

Taking the two dimensional Fourier transform of Eq. (3.43) leads to the transbilayer part of the form factor,

$$F_T = \int_{-\frac{D}{2}}^{\frac{D}{2}} \int_{-\frac{\lambda_r}{2}}^{\frac{\lambda_r}{2}} [\rho(x, z) - \rho_W] e^{i(q_x x + q_z z)} dx dz \quad (3.44)$$

$$= F_G + F_S + F_B. \quad (3.45)$$

The form factor is calculated in the minus fluid convention, where the bilayer electron

density is measured with respect to the electron density of the surrounding solvent. The expression for  $F_T$  is rather messy, so the derivation and full expression are in the appendix. Here, we note that the fitting parameters in this model are  $Z_{Hi}$ ,  $\sigma_{Hi}$ , and  $R_{HiM}$  for each of the two headgroup Gaussian functions,  $\sigma_M$  for the terminal methyl Gaussian,  $\Delta R$  for the methylene region,  $\psi$  for the lipid tilt, and an overall scaling factor. The contour part of the form factor has four more parameters ( $A$ ,  $x_M$ ,  $f_1$ , and  $f_2$ ). In total, the modified 2G hybrid model implements 14 structural parameters.

## 3.5 LAXS: results

### 3.5.1 Data and Electron Density Profile

Table 3.6 and 3.7 summarize observed intensity from data shown in Fig. 3.12.  $q_z$  values for observed peaks were corrected for index of refraction (Appendix B.4). We measured scattering on oriented samples in almost identical conditions as the best unoriented sample of Wack and Webb. As discussed earlier, these two types of samples have different Lorentz corrections, so this allowed us to check our data obtained on oriented samples against an unoriented sample. As Table 3.6 shows, agreement between our oriented data and the unoriented data was good, but integrated intensity from our oriented sample was in many cases slightly larger than that from the unoriented sample. We attribute this discrepancy to the way intensity was extracted. In an X-ray data from an oriented sample, each peak was nicely separated, so integrating a peak intensity was trivial. In contrast, some reflections in unoriented data were overlapping with each other (three pairs of overlapping peaks are highlighted in Table 3.6), making separation of intensity difficult. If the (1, 0) peak in the unoriented data had been overestimated, that would account for the observed discrepancy. Indeed, the microdensitometer trace in [8] suggests that the (1, 0) and (1, 1) reflections could have similar intensity as we observed in our oriented sample.

Figure 3.26 plots a two dimensional electron density profile calculated using the phases obtained from the M1G model and our experimental form factors. It is clear that the terminal methyl exists along the bilayer center in the major arm. The thickness along the local bilayer normal in the major arm was about 40 Å. This value is slightly larger than the previously published value of 37.9 Å obtained from the unoriented data [87]. The DMPC gel phase profile published in [53] also has shown that the distance between the headgroup centers in opposing monolayers is approximately 38 Å. Therefore, our experimental electron density profile suggests that chains in the ripple major arm are less tilted than in the gel phase, where chains are tilted by 30°. Incidentally, the maximum peak in the gel phase headgroup corresponding to the phosphate and choline components has been shown to be located at 20 Å from the bilayer center [53].

Figure 3.26 also shows absence of the terminal methyl trough in the minor arm. This absence is consistent with chains being interdigitated like in ref. [95]. Indeed, our electron density profile shows a small peak at the bilayer center of the minor

$h$	$k$	$q_z$ (Å $^{-1}$ )	$q_r$ (Å $^{-1}$ )	$I_{hk}^{\text{obs}}$	box size (pixels)	$h$	$k$	$q^*$ (Å $^{-1}$ )	oriented $ F_{hk} $	unoriented $ F_{hk} ^*$
1	-1	0.102	-0.043	726	10 $\times$ 7	1	-1	0.111	83.0	60.8
1	0	0.109	0.000	180818	10 $\times$ 7	1	0	0.108	100.0	100.0
1	1	0.114	0.043	241	10 $\times$ 7	1	1	0.123	44.0	26.9
1	3	0.128	0.130	4.8	10 $\times$ 7	1	3	0.185	9.9	7.6
2	-2	0.206	-0.087	51.4	10 $\times$ 7	2	-2	0.224	19.4	15.1
2	-1	0.212	0.044	1818	10 $\times$ 7	2	-1	0.215	80.2	71.2
2	0	0.218	0.000	10200	10 $\times$ 7	2	0	0.217	30.8	39.7
2	1	0.224	0.043	558	10 $\times$ 7	2	1	0.228	42.4	33.9
2	2	0.231	0.086	116	10 $\times$ 7	2	2	0.246	26.8	22.7
2	3	0.23	0.129	27	10 $\times$ 7	2	3	0.271	15.6	14.2
2	4	0.243	0.173	7.6	10 $\times$ 7	2	4	0.301	9.5	7.8
2	5	0.250	0.214	2.9	10 $\times$ 7	2	5	0.329	6.4	
3	-2	0.314	-0.087	305	15 $\times$ 7	3	-2	0.325	36.2	29.3
3	-1	0.321	-0.043	1205	15 $\times$ 7	3	-1	0.322	50.0	44.2
3	0	0.326	0.000	1566	15 $\times$ 7	3	0	0.325	14.4	12.0
3	1	0.333	0.043	31.7	15 $\times$ 7	3	1		7.9	
3	2	0.339	0.086	32.4	15 $\times$ 7	3	2	0.350	11.2	10.5
3	3	0.345	0.129	38.2	15 $\times$ 7	3	3	0.370	14.8	14.9
3	4	0.352	0.172	26.1	15 $\times$ 7	3	4	0.394	13.9	10.0
3	5	0.358	0.215	8.6	15 $\times$ 7	3	5		8.8	

Table 3.6: Observed intensity for  $h = 1$  to 3 at  $D = 57.8$ ,  $\lambda_r = 145$ , and  $\gamma = 98.2^\circ$ .

\*Unoriented data are from Wack and Webb [8].

$h$	$k$	$q_z$ (Å $^{-1}$ )	$q_r$ (Å $^{-1}$ )	$I_{hk}^{\text{obs}}$	box size (pixels)	$h$	$k$	oriented $ F_{hk} $
4	-3	0.417	-0.131	143	20 by 8	4	-3	25.7
4	-2	0.423	-0.087	730	20 by 8	4	-2	46.8
4	-1	0.429	-0.043	415	20 by 8	4	-1	24.7
4	0	0.435	0.000	1938	20 by 8	4	0	18.1
4	1			51.5	20 by 8	4	1	8.5
4	2	0.448	0.085	39	20 by 8	4	2	10.4
4	3			weak		4	3	
4	4	0.461	0.173	2.1	20 by 8	4	4	3.4
4	5	0.467	0.215	3.2	20 by 8	4	5	4.6
4	6	0.473	0.259	1.0	20 by 8	4	6	2.8
5	-3	0.525	-0.132	84.4	25 by 9	5	-3	17.3
5	-2	0.532	-0.087	146	25 by 9	5	-2	18.4
5	-1	0.538	-0.042	64.6	25 by 9	5	-1	8.5
5	0	0.544	0.000	259	25 by 9	5	0	7.3
5	1	0.550	0.040	50.2	25 by 9	5	1	7.2
6	-4	0.628	-0.175	10.3	30 by 10	6	-4	6.3
6	-3	0.635	-0.131	13.8	30 by 10	6	-3	6.3
6	-2	0.641	-0.085	9.7	30 by 10	6	-2	4.2
6	-1	0.647	-0.043	2.0	30 by 10	6	-1	0.0
6	0	0.653	0.000	69.0	30 by 10	6	0	4.1
6	1	0.659	0.043	2.5	30 by 10	6	1	0.0
6	2			weak		6	2	weak
6	3	0.672	0.128	42	30 by 10	6	3	10.5
6	4	0.679	0.170	40	30 by 10	6	4	11.7
7	-4	0.737	-0.174	42	35 by 10	7	-4	11.6
7	-3	0.743	-0.130	40	35 by 10	7	-3	9.7
7	-2	0.749	-0.085	15	35 by 10	7	-2	4.8
7	-1	0.755	-0.042	27	35 by 10	7	-1	4.5
7	0	0.760	0.000	41	35 by 10	7	0	3.4
9	-5			weak		9	-5	
9	-4	0.951	-0.174	19	35 by 10	9	-4	
9	-3			weak		9	-3	
9	-2	0.963	-0.085	21.0	35 by 10	9	-2	
9	-1			weak		9	-1	
9	0	0.974	0.000	21.0	35 by 10	9	0	

Table 3.7: Observed intensity for  $h = 4$  to 9 at  $D = 57.8$ ,  $\lambda_r = 145$ , and  $\gamma = 98.2^\circ$  (continued from Table 3.6).

arm, rather than depletion of electron density as in the gel and fluid phases. We also fitted the data to M1G models with more fitting parameters that allow the model parameters in the minor arm to be different from those in the major arm. In those cases also, we observed the same absence of the terminal methyl trough. However, when  $f_2$  was fixed to zero in the M1G model, we obtained a quite different profile, plotted in Fig. 3.27. There, the electron density shows a dip at the center of the bilayer in the minor arm, a usual feature seen in the fluid phase. Also, the headgroup in the minor arm appears to be more smooth compared to the profile shown in Fig. 3.26. Although the profile in Fig. 3.27 was obtained using a model yielding a worse chi-squared value, some features are seen to be more physical. Therefore, we argue that the ripple profile is closer to the one plotted in Fig 3.27 than that in Fig 3.26. It is quite mysterious as to why fixing or freeing the parameter  $f_2$  led to quite different profiles because this parameter was implemented to affect only the kink region. It may be that even higher order reflections than ones we observed might be necessary to obtain a robust minor arm profile. Since  $h = 9$  was quite strong, we expect to see more orders with the same instrument by simply probing a larger  $q$ -space.

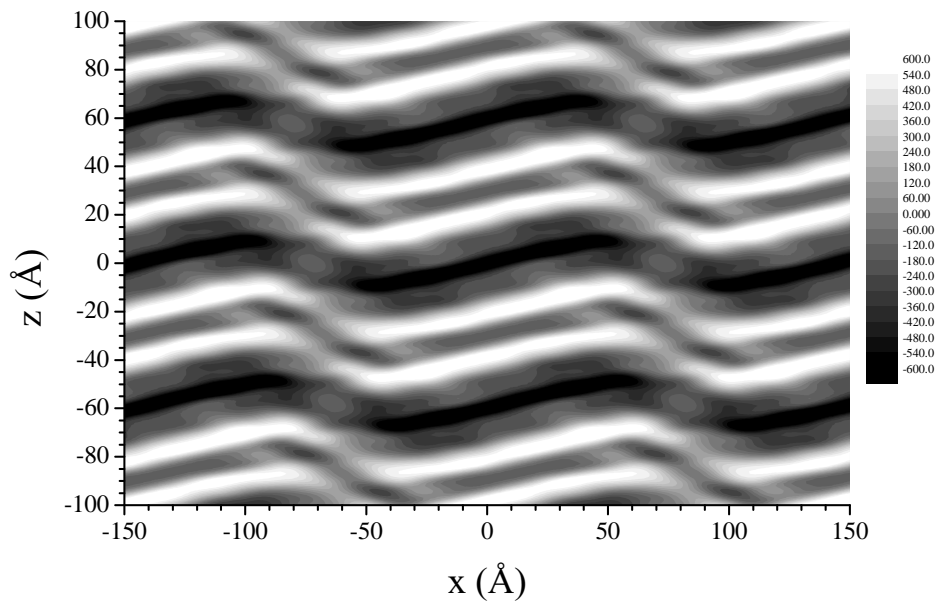


Figure 3.26: Electron density profile calculated using the phases obtained from the M2G model and experimental form factors. White is most electron dense and black is least electron dense. The thickness along the local bilayer normal in the major arm was about 40 Å. Depletion of electron density due to the terminal methyl is visible in the major arm but not in the minor arm.

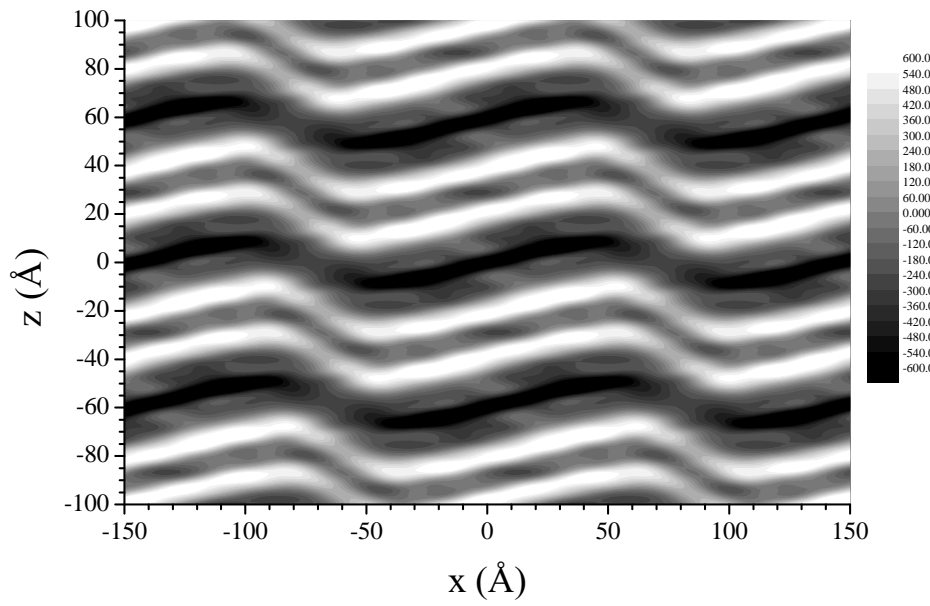


Figure 3.27: Electron density profile calculated using the phases obtained from the M2G model with  $f_2 = 0$  and experimental form factors. White is most electron dense and black is least electron dense. The thickness along the local bilayer normal in the major arm was about 40 Å. Depletion of electron density due to the terminal methyl is visible in the major arm but not in the minor arm.

### 3.6 NGIWAXS: results

Figure 3.28 shows near grazing incidence Wide Angle X-ray scattering (NGIWAXS) from an oriented DMPC film in the ripple phase. As can be seen, chain scattering did not vary considerably between the two  $D$ -spacings. A weak feature that looks like an arc coming from the chain peak was observed. This feature extended from  $\phi = 0^\circ$  to at least  $70^\circ$ . This feature is perhaps mosaic spread scattering. Figure 3.29 shows an enlarged view of the image shown in Fig. 3.28 for  $D = 60.8 \text{ \AA}$ . We observed a stronger peak off the equator and a weaker one, the center of which was not determined. The maximum intensity of the stronger peak was at  $(q_r, q_z) \approx (1.48 \text{ \AA}^{-1}, 0.20 \text{ \AA}^{-1})$  as shown in Fig. 3.30. The weaker peak was observed near the equator, and separation of this peak from the stronger one was most visible at  $q_z = 0.12 \text{ \AA}^{-1}$  as Fig. 3.31 shows. Because of absorption of X-rays due to the sample, intensity near the equator was not reliable. Therefore, we could not eliminate a possibility that the weaker peak is centered at  $q_z = 0 \text{ \AA}^{-1}$ . Nonetheless, Fig. 3.31 shows existence of more than one peak. Figure 3.32 shows many more  $q_r$  swaths.

Figure 3.33 shows NGIWAXS data from the DMPC gel phase. The width of (2,0) peak was the same as the instrumental resolution, indicating that the correlation of chains extends over a long distance. In contrast, the observed peaks in the ripple phase were much wider, suggesting that the correlation length in the ripple phase is much shorter. This observation is consistent with the finding in the electron density profile that chain packing in two different arms is different, thereby restricting the longest possible correlation along the ripple direction to be about  $100 \text{ \AA}$  in the major arm and  $50 \text{ \AA}$  in the minor arm. Although it is possible that the correlation length along the direction perpendicular to the ripple direction is long, this correlation length cannot be measured separately from the shorter one in our in-plane powder sample. For that, a single crystal sample would be required.

Figure 3.34 shows NGIWAXS of the DMPC fluid and ripple phases. Both images were collected from the same sample in the 2011 CHESS run with a low resolution setup. Figure 3.35 compares these data quantitatively. As can be seen, the maximum intensity of the fluid phase WAXS was observed at  $q_r \sim 1.4 \text{ \AA}^{-1}$ , slightly smaller  $q$  than the ripple peaks. The intensity of the fluid phase WAXS was scaled so that it lies below the ripple phase peak. While it is possible to argue that the long tail of the ripple peak is due to fluid like chain correlation in the minor arm, subtraction

of the fluid phase WAXS from the ripple phase WAXS results in a underlining ripple peak that is asymmetric (see Fig. 3.36). Therefore, chain packing in the minor arm is likely to be different from that in the fluid phase.

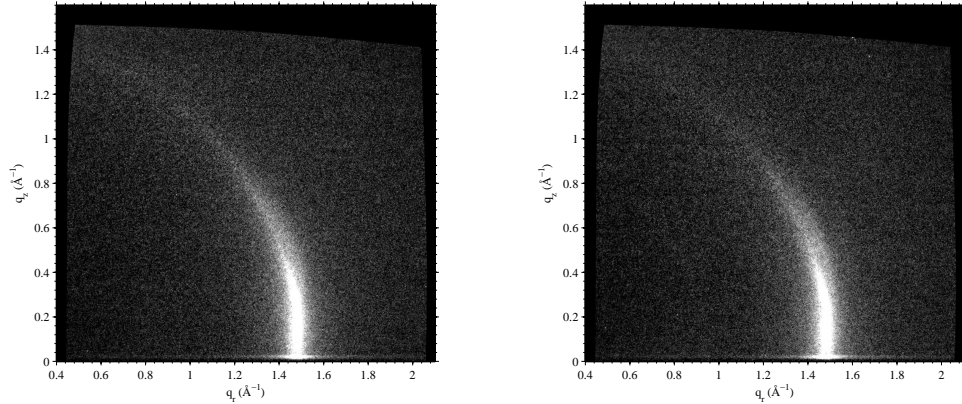


Figure 3.28: NGIWAXS of the DMPC ripple phase for  $D = 59.2 \text{ \AA}$  (left) and  $60.8 \text{ \AA}$  (right). The angle of incidence  $\omega$  was  $0.2^\circ$ . The black regions around the edge of each image are the  $q$ -space that was not probed. The distorted, non rectangular shape of the probed  $q$ -space signifies non-linear relation between the CCD space and sample  $q$ -space.

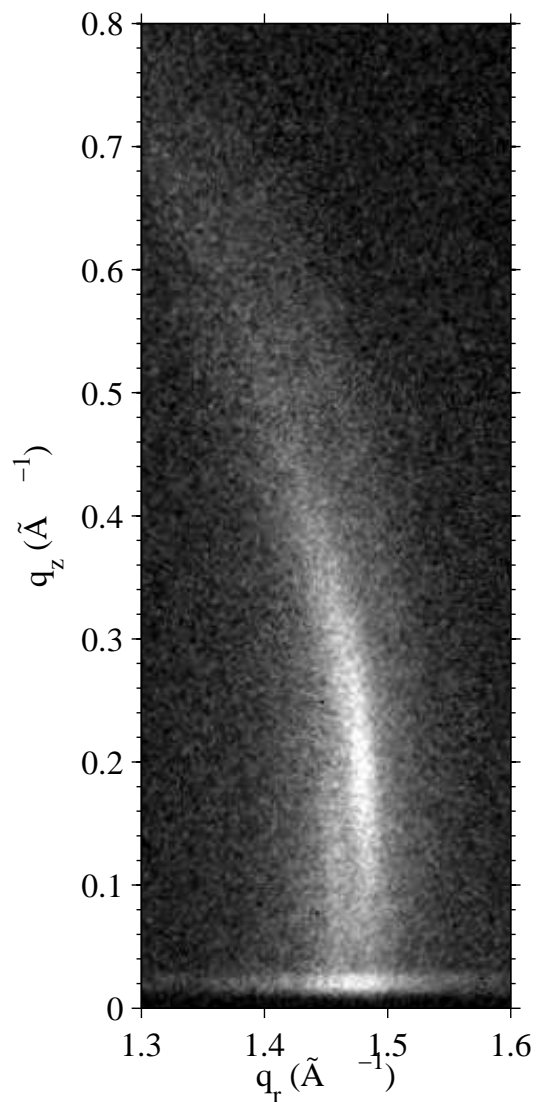


Figure 3.29: Enlarged view of the right image in Fig. 3.28. To show smaller features around the peak, a different contrast is used.

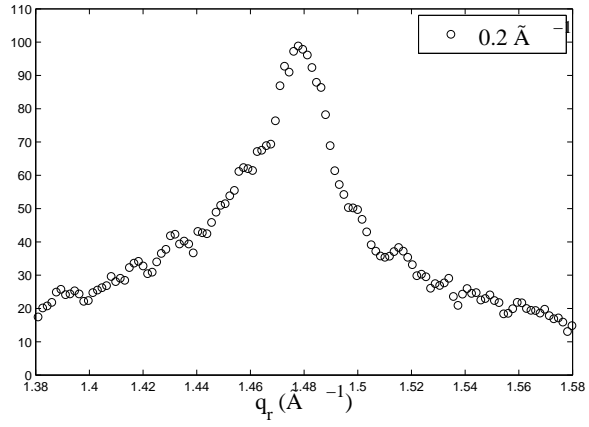


Figure 3.30:  $q_r$  swath averaged over  $0.02 \text{ \AA}^{-1}$  centered at  $q_z = 0.20 \text{ \AA}^{-1}$ , showing the maximum intensity of the stronger peak.

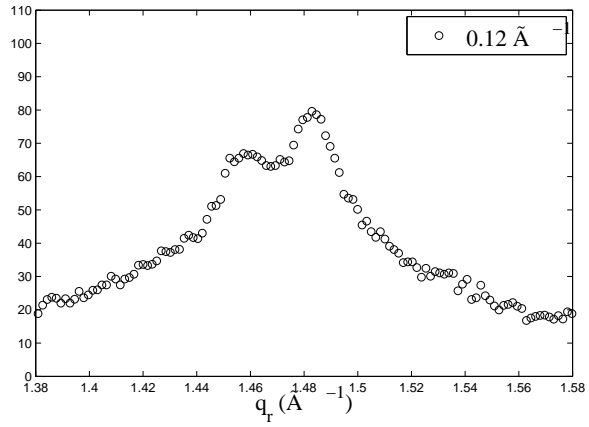


Figure 3.31:  $q_r$  swath averaged over  $0.02 \text{ \AA}^{-1}$  centered at  $q_z = 0.12 \text{ \AA}^{-1}$ , showing the weaker peak

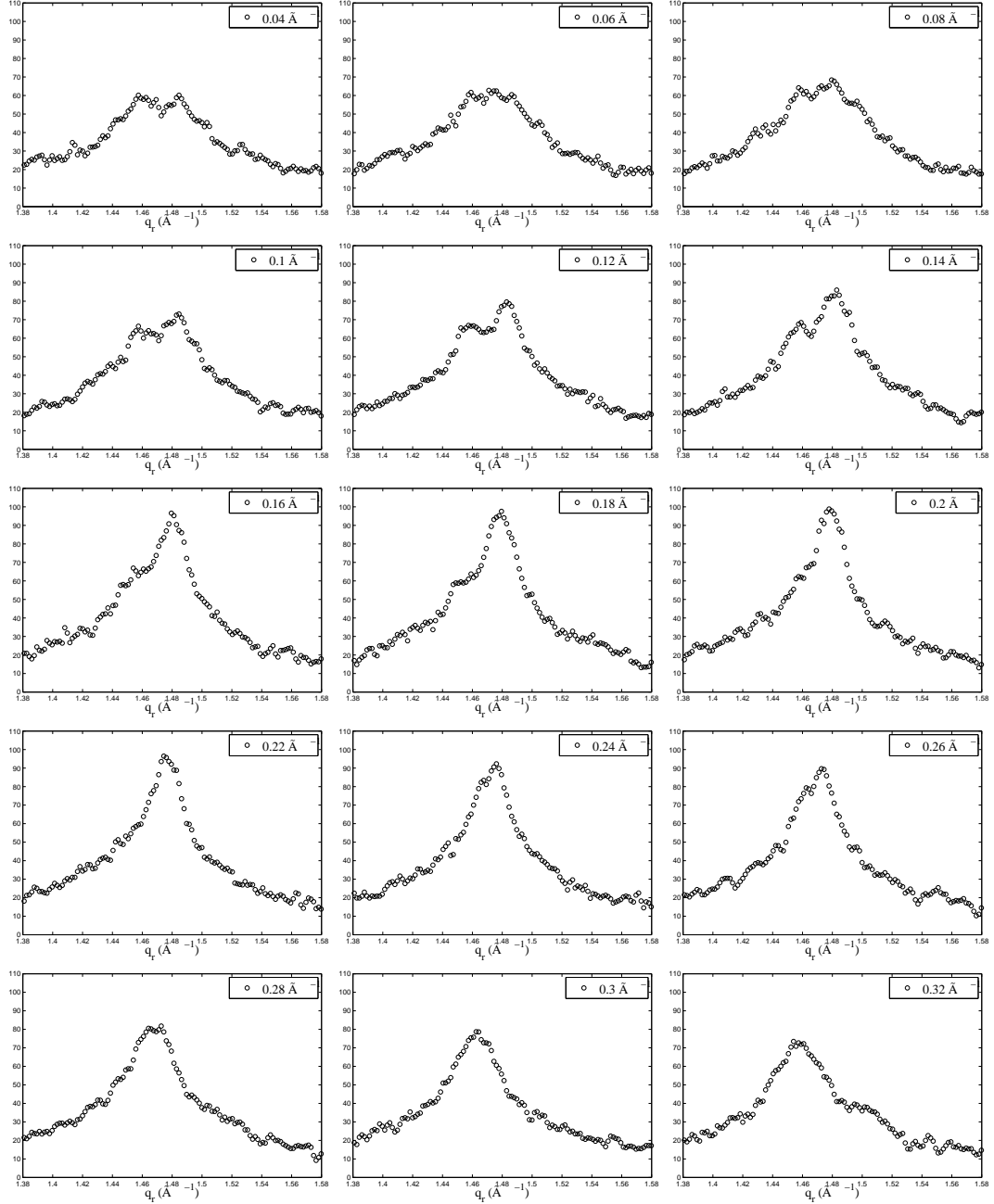


Figure 3.32:  $q_r$  swaths, each averaged over  $0.02 \text{ \AA}^{-1}$ . The center  $q_z$  value of a swatch is shown in the figure legends.

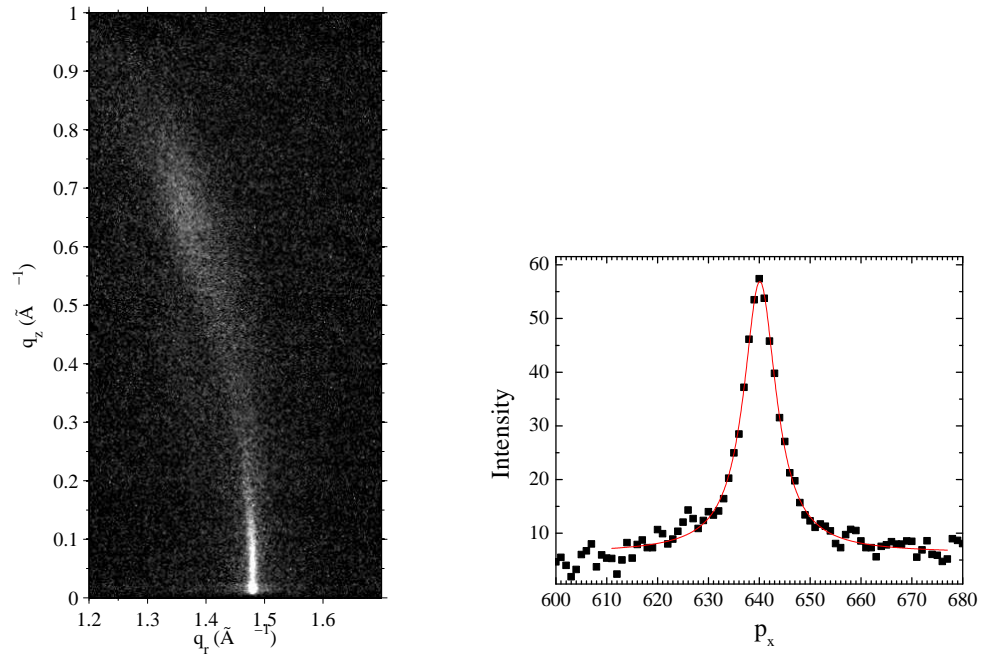


Figure 3.33: (left) NGIWAXS image of the DMPC gel phase at 10 °C for  $D = 57.7 \text{ \AA}$ . The (2,0) peak was at  $q_r = 1.479 \text{ \AA}^{-1}$ , corresponding to  $d_{20} = 4.25 \text{ \AA}$ . (right) The (2,0) peak plotted along horizontal pixels  $p_x$  averaging over 8 pixels in  $p_z$ . The solid red line is a Lorentzian fit to the data, resulting in the FWHM of  $\sim 8$  pixels, corresponding to  $\Delta q = 0.014 \text{ \AA}^{-1}$ . which is an unresolved width of intrinsically infinitely sharp peak estimated in Sec. 3.2.2.

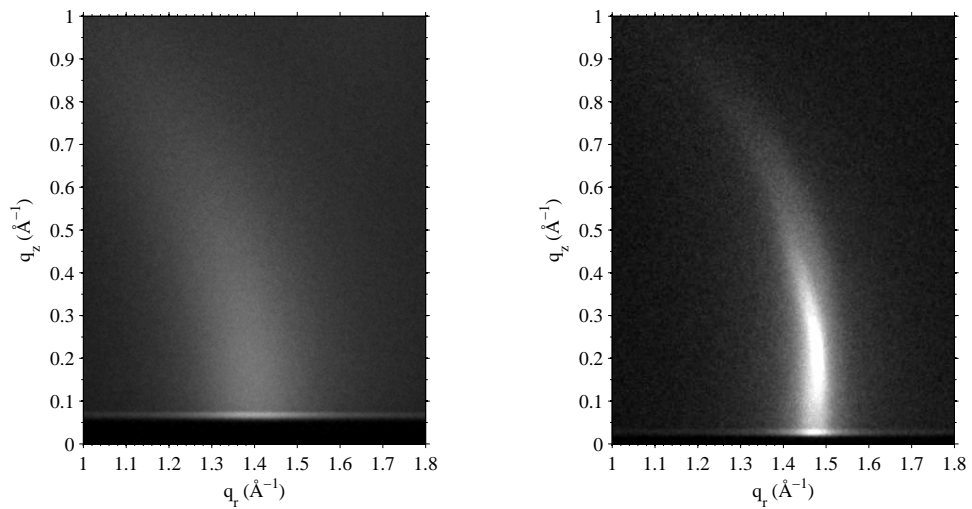


Figure 3.34: (left) NGIWAXS of the DMPC fluid phase at 30 °C.  $\omega = 0.5^\circ$ . The data were taken in the 2011 run with a low resolution setup. The sample width,  $w_s = 2$  mm. (right) NGIWAXS of the DMPC ripple phase at 18 °C.  $\omega = 0.2^\circ$ . The data were also taken in 2011 with a low resolution setup.  $w_s = 2$  mm.

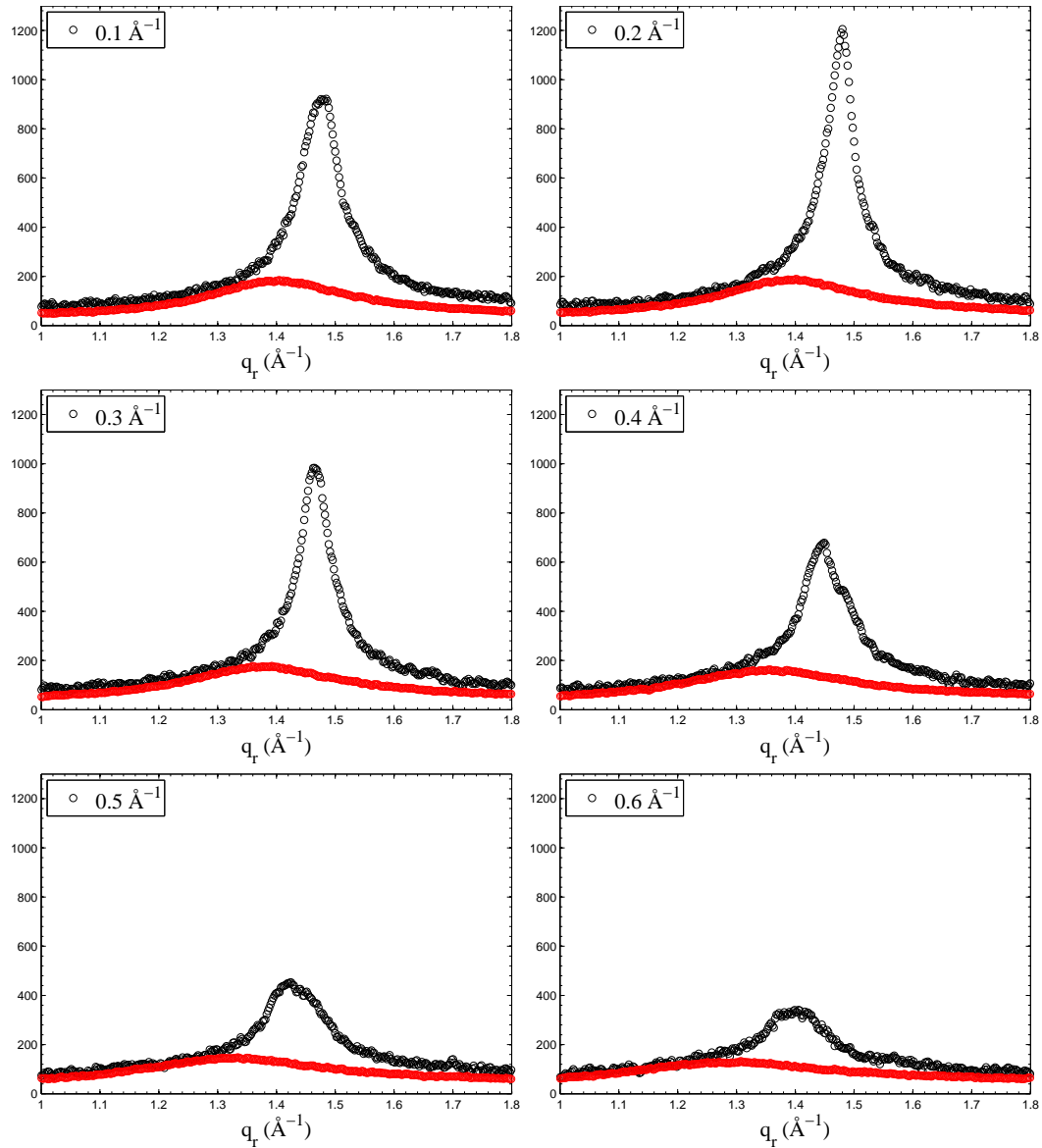


Figure 3.35:  $q_r$  swaths comparing intensity of the fluid WAXS and ripple WAXS. The fluid phase data were scaled so that its WAXS lies below the ripple WAXS.

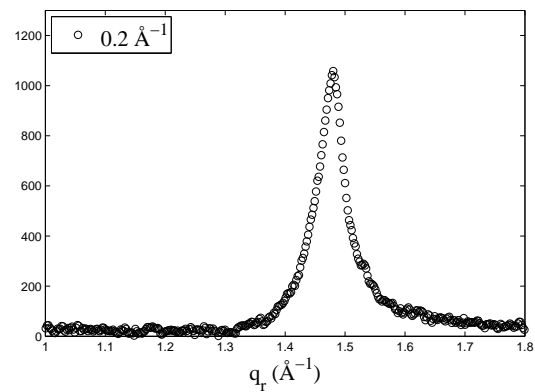


Figure 3.36: Subtraction of the fluid phase WAXS from the ripple phase WAXS. The subtraction results in asymmetric ripple peak.

## 3.7 TWAXS: results

Figure 3.37 shows the transmission wide angle X-ray scattering pattern after the CCD to  $q$  transformation. The stronger peak observed in NGIWAXS was also observed at approximately the same location. Because of a larger instrumental resolution than in the NGIWAXS experiment, the weaker peak was not well separated. Figure 3.38 shows a slight hint of the weak peak at  $q_z = 0.12 \text{ \AA}^{-1}$  and Fig. 3.39 shows many more  $q_r$  swaths. This data set taken in the 2011 run motivated me to try an experiment with a higher instrumental resolution, which led to the NGIWAXS experiment in the 2013 run. Figure 3.40 shows intensity along  $q_z$ , averaged between  $1.46 \text{ \AA}^{-1}$  and  $1.52 \text{ \AA}^{-1}$ . It shows absence of a sharp peak at  $q_z = 0 \text{ \AA}^{-1}$ , complementing the NGIWAXS data. While the instrumental resolution here was not great, Fig. 3.39 and 3.40 indicate that the second, weaker peak is located at or above  $q_z = 0.12 \text{ \AA}^{-1}$ .

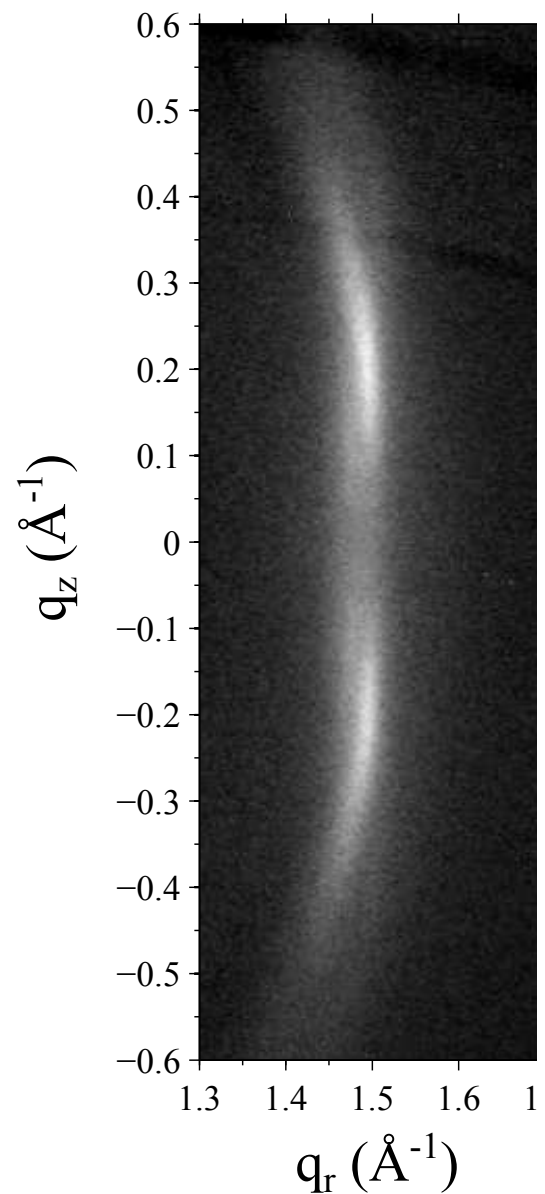


Figure 3.37: TWAXS image of the DMPC ripple phase at 18 °C and  $D = 60.3 \text{ \AA}$ .

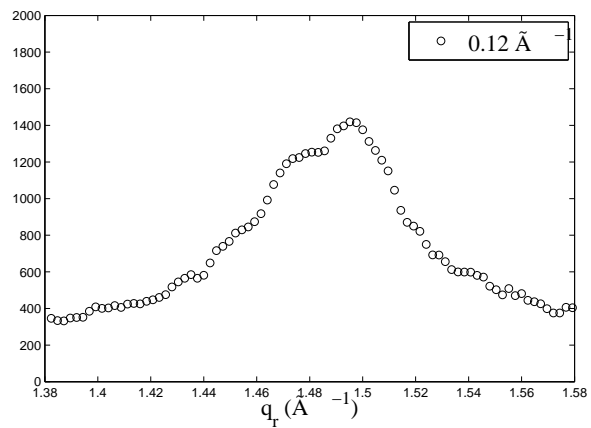


Figure 3.38:  $q_r$  swath of the TWAXS image averaged over  $0.02 \text{ \AA}^{-1}$  centered at  $q_z = 0.12 \text{ \AA}^{-1}$ .

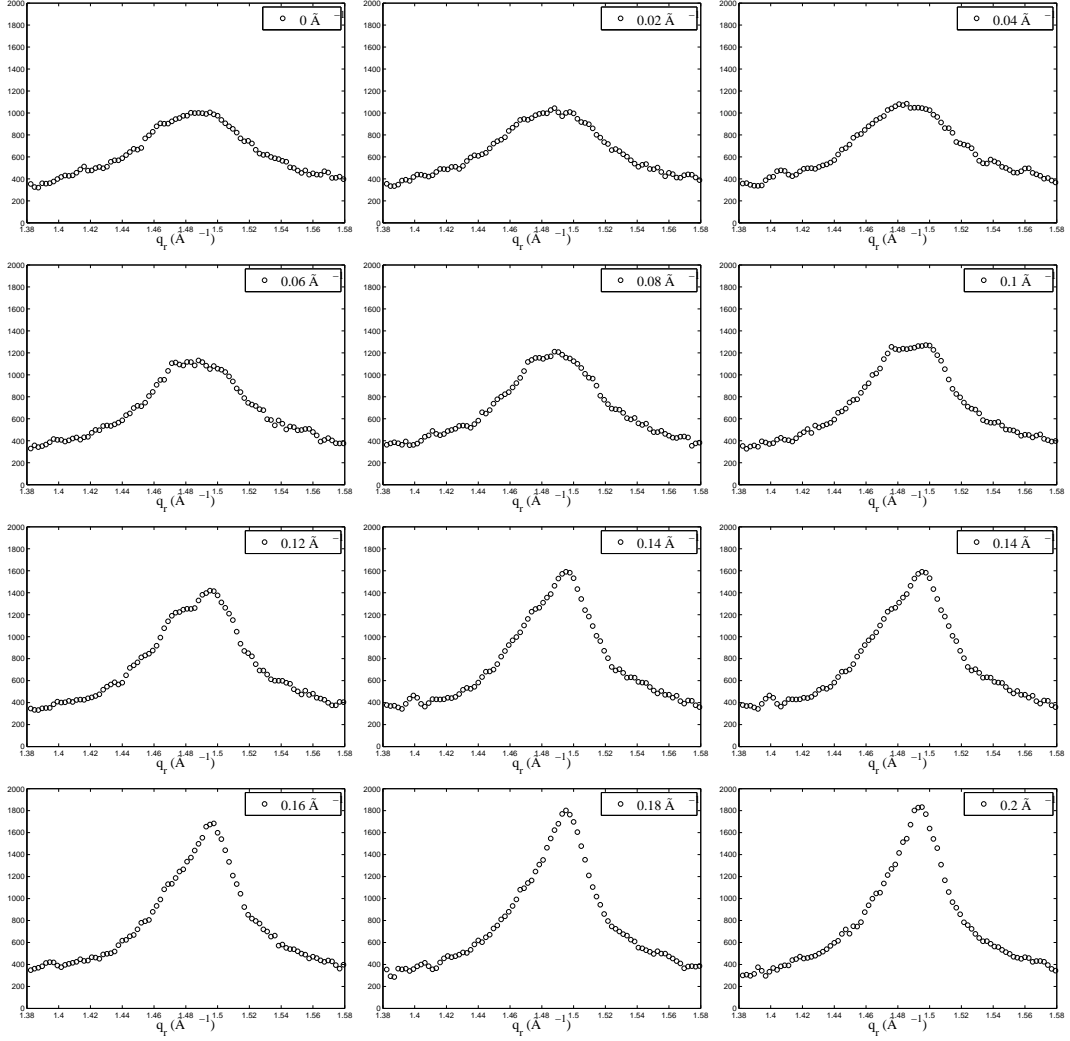


Figure 3.39:  $q_r$  swaths of the TWAXS image, each averaged over  $0.02 \text{ \AA}^{-1}$ . The center  $q_z$  value of a swatch is shown in the figure legends.

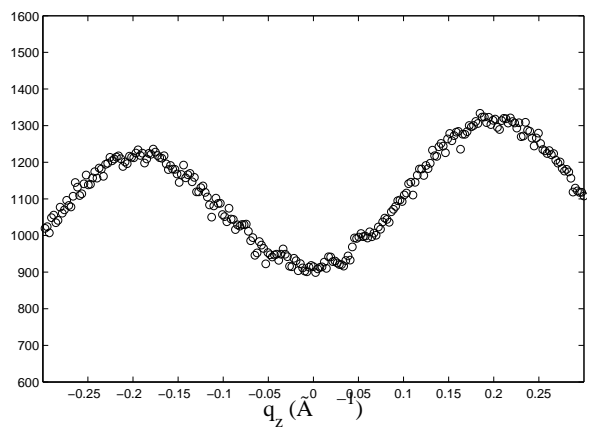


Figure 3.40:  $q_z$  swath averaged between  $1.46 \text{ \AA}^{-1}$  and  $1.52 \text{ \AA}^{-1}$ .

## 3.8 Discussion

The ripple phase has attracted many researchers since its discovery in 1967, and extensive structural work on average structural properties such as the ripple wavelength, oblique angle,  $D$ -spacing, and electron density profiles have been published. From those experimental measurements, many theoretical models to explain the origin of the ripple phase have been published with some models resulting in predictions inconsistent with the experimental data. Yet, from equilibrium structural study such as X-ray scattering, chain packing for the asymmetric ripple has only been suggested based on the measured thicknesses of the major and minor arms. For example, based on the calculated electron density profile, Sun *et al.* [87] has suggested that the chains in the minor arm are disordered like in the fluid phase. Sengupta *et al.* [99] has argued, also based on the electron density profile calculated using the data by Wack and Webb, that chains are packed like in the gel phase throughout both arms with the same tilt angle with respect to the stacking  $z$  direction. Since the thickness of the major arm has shown to be almost the same as that of the gel phase, they argued that chains in the major arm should be tilted about 30° with respect to the bilayer local normal.

Since the millennium, a few simulations have predicted different type of chain packing. For example, all atomistic simulations done by de Vrie *et al.* [95] have predicted existence of interdigitated state in the minor arm of the DMPC asymmetric ripple while lipids in the major arm are packed like in the gel phase with the monolayers decoupled from each other.

Previous predictions and suggestions so far have not been able to directly be verified because of the lack of quantitative wide angle scattering data. Although the DMPC WAXS was measured by Katsaras and Raghunathan [100] using a rotating anode, the wide angle peak measured was broad and ambiguous to answer the question of lipid packing. Therefore, we sought to fill the gap with synchrotron X-ray, which has been successful in describing the fluid phase chain-chain correlation. Our strength were three fold: 1) brilliant synchrotron beam that allowed use of Si monochromator with a very small energy dispersion, 2) stacks of ~2000 bilayers oriented on the substrate that scattered strongly and anisotropically, and 3) hydration chamber that allowed us to control the hydration of the sample.

By careful analysis of low angle X-ray scattering data, we have shown that chains

in the major arm are straightened like in the gel phase, the finding of which is consistent with previous publications. The thickness of the major arm was measured to be 40 Å, slightly larger than the previously published value of 37.9 Å [87]. The electron density profile in the minor arm we obtained was similar to that of interdigitated chains. However, the wide angle X-ray scattering data is inconsistent with this. As de Vries *et. al.* calculated, interdigitated chains in the minor arm would result in a wide angle peak at  $q_z \approx 0.5 \text{ \AA}^{-1}$ , much larger  $q_z$  than 0.2 Å<sup>-1</sup> that we observed.

By comparing the wide angle pattern from the ripple and fluid phases, we showed that scattering intensity around 1.4 Å<sup>-1</sup> in the ripple phase is probably the tail of the stronger peak coming from the major arm and not due to the fluid-like chain packing in the minor arm.

Given existence of gel-like packing in the major arm, we argue that the stronger peak observed in the NGIWAXS data is the Bragg rod from the major arm. It is not clear, however, whether or not the weaker peak is also due to packing in the major arm. Resolving this issue seems to require modeling of various types of chain packing for both major and minor arms.

### 3.9 Conclusion

We have attempted to solve the lateral structure of the lipids within the bilayer using synchrotron X-rays. While we could not calculate the electron density profile unambiguously or solve the chain packing based on the measured wide angle scattering data, previously suggested structure of the ripple phase can be tested against our data. For example, Monte Carlo simulations based on a model free energy can be tuned to obtain a good fit to our measured wide angle data. One could also consider some exotic packing such as swirling pattern observed by Watkin et al. (PNAS) or tilt modulation field. Predicting the scattering intensity pattern from these structures might lead to a different way to analyze our LAXS and NGIWAXS data and possibly more improved study of the ripple phase.

Future possible experiments include a high resolution transmission experiment, where both geometric broadening and energy dispersion are minimized. The expected resolution is the width of the X-ray beam, which is about 3 pixels. This experiment doubles the best resolution achieved in this work. Another slightly different high resolution experiment is to use silicon crystal analyzer downstream of the

sample, which completely remove geometric broadening. The downside of this type of high resolution experiment is that only one point in q-space is probed at any given exposure, so getting a full 2D map of wide angle scattering is time consuming.

Also highly speculative, but the ripple phase might be an interesting phase to study curvature sensing peptides. The description of curvature in the ripple phase has been around for a while. Those curvature sensing peptides may accumulate at the kink regions. Then, the electron density profile can be calculated with the analysis detailed in this work. It would be very interesting if peptide-lipid interactions also significantly modify the wide angle pattern. With a known perturbation property of a peptide on lipids, it could shed light on the structure of the minor arm. For example, if indeed chains are fluid like in the minor, some peptides might have tendency to accumulate in the minor arm because of ease of insertion compared to the gel-like major arm. Then, the ripple phase might be used to study biologically relevant problems.

# Appendices

# Bibliography

- [1] PF Fahey and WW Webb. Lateral diffusion in phospholipid bilayer membranes and multilamellar liquid crystals. *Biochemistry*, 17(15):3046–3053, 1978.
- [2] A. Tardieu, Vittorio Luzzati, and F.C. Reman. Structure and polymorphism of the hydrocarbon chains of lipids: A study of lecithin-water phases. *Journal of Molecular Biology*, 75(4):711 – 733, 1973.
- [3] Elizabeth J Luna and Harden M McConnell. The intermediate monoclinic phase of phosphatidylcholines. *Biochimica et Biophysica Acta (BBA)-Biomembranes*, 466(3):381–392, 1977.
- [4] Bruce R. Copeland and Harden M. McConnel. The rippled structure in bi-layer membranes of phosphatidylcholine and binary mixtures of phosphatidyl-choline and cholesterol. *Biochimica et Biophysica Acta (BBA) - Biomembranes*, 599(1):95 – 109, 1980.
- [5] D Ruppel and E Sackmann. On defects in different phases of two-dimensional lipid bilayers. *Journal de Physique*, 44(9):1025–1034, 1983.
- [6] JAN Zasadzinski and MB Schneider. Ripple wavelength, amplitude, and configuration in lyotropic liquid crystals as a function of effective headgroup size. *Journal de Physique*, 48(11):2001–2011, 1987.
- [7] JA Zasadzinski, J Schneir, J Gurley, V Elings, and PK Hansma. Scanning tunneling microscopy of freeze-fracture replicas of biomembranes. *Science*, 239(4843):1013–1015, 1988.
- [8] Daniel C. Wack and Watt W. Webb. Synchrotron x-ray study of the modulated lamellar phase  $p\beta'$  in the lecithin-water system. *Phys. Rev. A*, 40:2712–2730, Sep 1989.

- [9] RJ Wittebort, CF Schmidt, and RG Griffin. Solid-state carbon-13 nuclear magnetic resonance of the lecithin gel to liquid-crystalline phase transition. *Biochemistry*, 20(14):4223–4228, 1981.
- [10] Marilyn B Schneider, WINSTON K Chan, and Watt W Webb. Fast diffusion along defects and corrugations in phospholipid p beta, liquid crystals. *Biophysical journal*, 43(2):157–165, 1983.
- [11] Martin J. Janiak, Donald M. Small, and G. Graham Shipley. Nature of the thermal pretransition of synthetic phospholipids: dimyristoyl- and dipalmitoyl-lecithin. *Biochemistry*, 15(21):4575–4580, 1976.
- [12] Rainer Fischer, Mariola Fotin-Mleczek, Hansjrg Hufnagel, and Roland Brock. Break on through to the other sidebiophysics and cell biology shed light on cell-penetrating peptides. *ChemBioChem*, 6(12):2126–2142, 2005.
- [13] Alain Joliot and Alain Prochiantz. Transduction peptides: from technology to physiology. *Nat Cell Biol*, 6(3), 2004.
- [14] Maria Lindgren, Mattias Hillbrink, Alain Prochiantz, and lo Langel. Cell-penetrating peptides. *Trends in Pharmacological Sciences*, 21(3):99 – 103, 2000.
- [15] Alan D. Frankel and Carl O. Pabo. Cellular uptake of the tat protein from human immunodeficiency virus. *Cell*, 55(6):1189 – 1193, 1988.
- [16] Maurice Green and Paul M. Loewenstein. Autonomous functional domains of chemically synthesized human immunodeficiency virus tat trans-activator protein. *Cell*, 55(6):1179 – 1188, 1988.
- [17] Eric Viks, Priscille Brodin, and Bernard Lebleu. Hiv-1 tat protein basic domain rapidly translocates through the plasma membrane and accumulates in the cell nucleus. *Journal of Biological Chemistry*, 272(25):16010–16017, 1997.
- [18] Gohar Ter-Avetisyan, Gisela Tnnemann, Danny Nowak, Matthias Nitschke, Andreas Herrmann, Marek Drab, and M. Cristina Cardoso. Cell entry of arginine-rich peptides is independent of endocytosis. *Journal of Biological Chemistry*, 284(6):3370–3378, 2009.

- [19] Gisela Tnnemann, Robert M. Martin, Simone Haupt, Christoph Patsch, Frank Edenhofer, and M. Cristina Cardoso. Cargo-dependent mode of uptake and bioavailability of tat-containing proteins and peptides in living cells. *The FASEB Journal*, 20(11):1775–1784, 2006.
- [20] Andr Ziegler, Pierluigi Nervi, Markus Drrenberger, and Joachim Seelig. The cationic cell-penetrating peptide cpptat derived from the hiv-1 protein tat is rapidly transported into living fibroblasts: optical, biophysical, and metabolic evidence. *Biochemistry*, 44(1):138–148, 2005. PMID: 15628854.
- [21] J. S. Wadia, R. V. Stan, and S. F. Dowdy. Transducible tat-ha fusogenic peptide enhances escape of tat-fusion proteins after lipid raft macropinocytosis. *Nature Medicine*, 10(3):310–315, 2004.
- [22] I. M. Kaplan, J. S. Wadia, and S. F. Dowdy. Cationic tat peptide transduction domain enters cells by macropinocytosis. *Journal of Controlled Release*, 102(1):247–253, 2005.
- [23] David A Mann and Alan D Frankel. Endocytosis and targeting of exogenous hiv-1 tat protein. *The EMBO journal*, 10(7):1733, 1991.
- [24] Jean Philippe Richard, Kamran Melikov, Hilary Brooks, Paul Prevot, Bernard Lebleu, and Leonid V Chernomordik. Cellular uptake of unconjugated tat peptide involves clathrin-dependent endocytosis and heparan sulfate receptors. *Journal of Biological Chemistry*, 280(15):15300–15306, 2005.
- [25] Simon W Jones, Richard Christison, Ken Bundell, Catherine J Voyce, Sarah Brockbank, Peter Newham, and Mark A Lindsay. Characterisation of cell-penetrating peptide-mediated peptide delivery. *British journal of pharmacology*, 145(8):1093–1102, 2005.
- [26] Agnès Vendeville, Fabienne Rayne, Anne Bonhoure, Nadir Bettache, Philippe Montcourrier, and Bruno Beaumelle. Hiv-1 tat enters t cells using coated pits before translocating from acidified endosomes and eliciting biological responses. *Molecular biology of the cell*, 15(5):2347–2360, 2004.
- [27] Christina Foerg, Urs Ziegler, Jimena Fernandez-Carneado, Ernest Giralt, Robert Rennert, Annette G Beck-Sickinger, and Hans P Merkle. Decoding the

- entry of two novel cell-penetrating peptides in hela cells: lipid raft-mediated endocytosis and endosomal escape. *Biochemistry*, 44(1):72–81, 2005.
- [28] Antonio Fittipaldi and Mauro Giacca. Transcellular protein transduction using the tat protein of hiv-1. *Advanced drug delivery reviews*, 57(4):597–608, 2005.
- [29] Ying Liu, Melina Jones, Cynthia M Hingtgen, Guojun Bu, Nick Laribee, Rudolph E Tanzi, Robert D Moir, Avindra Nath, and Johnny J He. Uptake of hiv-1 tat protein mediated by low-density lipoprotein receptor-related protein disrupts the neuronal metabolic balance of the receptor ligands. *Nature medicine*, 6(12):1380–1387, 2000.
- [30] Vladimir P Torchilin, Ram Rammohan, Volkmar Weissig, and Tatyana S Levchenko. Tat peptide on the surface of liposomes affords their efficient intracellular delivery even at low temperature and in the presence of metabolic inhibitors. *Proceedings of the National Academy of Sciences*, 98(15):8786–8791, 2001.
- [31] Vladimir P Torchilin, Tatyana S Levchenko, Ram Rammohan, Natalia Volodina, Brigitte Papahadjopoulos-Sternberg, and Gerard GM D’Souza. Cell transfection in vitro and in vivo with nontoxic tat peptide-liposome–dna complexes. *Proceedings of the National Academy of Sciences*, 100(4):1972–1977, 2003.
- [32] Carsten Rudolph, Christian Plank, James Lausier, Ulrike Schillinger, Rainer H Müller, and Joseph Rosenecker. Oligomers of the arginine-rich motif of the hiv-1 tat protein are capable of transferring plasmid dna into cells. *Journal of Biological Chemistry*, 278(13):11411–11418, 2003.
- [33] Ashok Chauhan, Akshay Tikoo, Arvinder K Kapur, and Mahavir Singh. The taming of the cell penetrating domain of the hiv tat: myths and realities. *Journal of Controlled Release*, 117(2):148–162, 2007.
- [34] JM Sabatier, E Vives, K Mabrouk, ABDELAZIZ Benjouad, H Rochat, A Duval, B Hue, and ELMOSTAFA Bahraoui. Evidence for neurotoxic activity of tat from human immunodeficiency virus type 1. *Journal of virology*, 65(2):961–967, 1991.

- [35] A. Mishra, V. D. Gordon, L. H. Yang, R. Coridan, and G. C. L. Wong. Hiv tat forms pores in membranes by inducing saddle-splay curvature: Potential role of bidentate hydrogen bonding. *Angewandte Chemie-International Edition*, 47(16):2986–2989, 2008.
- [36] S. T. Yang, E. Zaitseva, L. V. Chernomordik, and K. Melikov. Cell-penetrating peptide induces leaky fusion of liposomes containing late endosome-specific anionic lipid. *Biophysical Journal*, 99(8):2525–2533, 2010.
- [37] P. E. G. Thoren, D. Persson, E. K. Esbjorner, M. Goksor, P. Lincoln, and B. Norden. Membrane binding and translocation of cell-penetrating peptides. *Biochemistry*, 43(12):3471–3489, 2004.
- [38] SD Krämer and H Wunderli-Allenspach. No entry for tat (44–57) into liposomes and intact mdck cells: novel approach to study membrane permeation of cell-penetrating peptides. *Biochimica et Biophysica Acta (BBA)-Biomembranes*, 1609(2):161–169, 2003.
- [39] C. Ciobanasu, J. P. Siebrasse, and U. Kubitscheck. Cell-penetrating hiv1 tat peptides can generate pores in model membranes. *Biophysical Journal*, 99(1):153–62, 2010.
- [40] Philip A Gurnev, Sung-Tae Yang, Kamran C Melikov, Leonid V Chernomordik, and Sergey M Bezrukov. Cationic cell-penetrating peptide binds to planar lipid bilayers containing negatively charged lipids but does not induce conductive pores. *Biophysical journal*, 104(9):1933–1939, 2013.
- [41] H. D. Herce, A. E. Garcia, J. Litt, R. S. Kane, P. Martin, N. Enrique, A. Rebolledo, and V. Milesi. Arginine-rich peptides destabilize the plasma membrane, consistent with a pore formation translocation mechanism of cell-penetrating peptides. *Biophysical Journal*, 97(7):1917–1925, 2009.
- [42] Y. C. Su, A. J. Waring, P. Ruchala, and M. Hong. Membrane-bound dynamic structure of an arginine-rich cell-penetrating peptide, the protein transduction domain of hiv tat, from solid-state nmr. *Biochemistry*, 49(29):6009–6020, 2010.

- [43] S. Shojania and J. D. O’Neil. Hiv-1 tat is a natively unfolded protein - the solution conformation and dynamics of reduced hiv-1 tat-(1-72) by nmr spectroscopy. *Journal of Biological Chemistry*, 281(13):8347–8356, 2006.
- [44] P. Bayer, M. Kraft, A. Ejchart, M. Westendorp, R. Frank, and P. Rosch. Structural studies of hiv-1 tat protein. *Journal of Molecular Biology*, 247(4):529–535, 1995.
- [45] H. D. Herce and A. E. Garcia. Molecular dynamics simulations suggest a mechanism for translocation of the hiv-1 tat peptide across lipid membranes. *Proceedings of the National Academy of Sciences of the United States of America*, 104(52):20805–20810, 2007.
- [46] S. Yesylevskyy, S. J. Marrink, and A. E. Mark. Alternative mechanisms for the interaction of the cell-penetrating peptides penetratin and the tat peptide with lipid bilayers. *Biophysical Journal*, 97(1):40–49, 2009.
- [47] SL Barna, MW Tate, SM Gruner, and EF Eikenberry. Calibration procedures for charge-coupled device x-ray detectors. *Review of Scientific Instruments*, 70(7):2927–2934, 1999.
- [48] Y. Lyatskaya, Y. F. Liu, S. Tristram-Nagle, J. Katsaras, and J. F. Nagle. Method for obtaining structure and interactions from oriented lipid bilayers. *Physical Review E*, 63(1):0119071–0119079, 2001.
- [49] Y. F. Liu and J. F. Nagle. Diffuse scattering provides material parameters and electron density profiles of biomembranes. *Physical Review E*, 69(4):040901–040904(R), 2004.
- [50] Yufeng Liu. *NEW METHOD TO OBTAIN STRUCTURE OF BIOMEMBRANES USING DIFFUSE -RAY SCATTERING: APPLICATION TO FLUID PHASE DOPC LIPID BILAYERS*. PhD thesis, Carnegie Mellon University, 2003.
- [51] John F Nagle and Stephanie Tristram-Nagle. Structure of lipid bilayers. *Biochimica et Biophysica Acta (BBA)-Reviews on Biomembranes*, 1469(3):159–195, 2000.

- [52] Norbert Kuerka, John F. Nagle, Jonathan N. Sachs, Scott E. Feller, Jeremy Pencer, Andrew Jackson, and John Katsaras. Lipid bilayer structure determined by the simultaneous analysis of neutron and x-ray scattering data. *Biophysical Journal*, 95(5):2356 – 2367, 2008.
- [53] Stephanie Tristram-Nagle, Yufeng Liu, Justin Legleiter, and John F. Nagle. Structure of gel phase DMPC determined by x-ray diffraction. *Biophysical Journal*, 83(6):3324 – 3335, 2002.
- [54] Anthony R. Braun, Jonathan N. Sachs, and John F. Nagle. Comparing simulations of lipid bilayers to scattering data: The gromos 43a1-s3 force field. *The Journal of Physical Chemistry B*, 117(17):5065–5072, 2013.
- [55] <http://seal.web.cern.ch/seal/documents/minuit/mnusersguide.pdf>.
- [56] <http://lcgapp.cern.ch/project/cls/work-packages/mathlibs/minuit/index.html>.
- [57] Berk Hess, Carsten Kutzner, David van der Spoel, and Erik Lindahl. Gromacs 4: Algorithms for highly efficient, load-balanced, and scalable molecular simulation. *Journal of Chemical Theory and Computation*, 4(3):435–447, 2008.
- [58] Joakim P. M. Jmbeck and Alexander P. Lyubartsev. Derivation and systematic validation of a refined all-atom force field for phosphatidylcholine lipids. *The Journal of Physical Chemistry B*, 116(10):3164–3179, 2012.
- [59] Joakim P. M. Jmbeck and Alexander P. Lyubartsev. An extension and further validation of an all-atomistic force field for biological membranes. *Journal of Chemical Theory and Computation*, 8(8):2938–2948, 2012.
- [60] Viktor Hornak, Robert Abel, Asim Okur, Bentley Strockbine, Adrian Roitberg, and Carlos Simmerling. Comparison of multiple amber force fields and development of improved protein backbone parameters. *Proteins: Structure, Function, and Bioinformatics*, 65(3):712–725, 2006.
- [61] W. L. Jorgensen, J. Chandrasekhar, J. D. Madura, R. W. Impey, and M. L. Klein. Comparison of simple potential functions for simulating liquid water. *Journal of Chemical Physics*, 79(2):926–935, 1983.

- [62] Norbert Kuerka, John Katsaras, and JohnF. Nagle. Comparing membrane simulations to scattering experiments: Introducing the simtoexp software. *Journal of Membrane Biology*, 235(1):43–50, 2010.
- [63] Shuichi Miyamoto and Peter A Kollman. Settle: an analytical version of the shake and rattle algorithm for rigid water models. *Journal of computational chemistry*, 13(8):952–962, 1992.
- [64] B. Hess, H. Bekker, H. J. C. Berendsen, and J. G. E. M. Fraaije. Lincs: A linear constraint solver for molecular simulations. *J Comput Chem*, 18(12):1463–1472, 1997.
- [65] Tom Darden, Darrin York, and Lee Pedersen. Particle mesh ewald: An  $n \log(n)$  method for ewald sums in large systems. *The Journal of chemical physics*, 98(12):10089–10092, 1993.
- [66] Giovanni Bussi, Davide Donadio, and Michele Parrinello. Canonical sampling through velocity rescaling. *The Journal of chemical physics*, 126(1):014101, 2007.
- [67] Michele Parrinello and Aneesur Rahman. Polymorphic transitions in single crystals: A new molecular dynamics method. *Journal of Applied physics*, 52(12):7182–7190, 1981.
- [68] Norbert Kučerka, Yufeng Liu, Nanjun Chu, Horia I Petrache, Stephanie Tristram-Nagle, and John F Nagle. Structure of fully hydrated fluid phase DMPC and DLPC lipid bilayers using X-ray scattering from oriented multilamellar arrays and from unilamellar vesicles. *Biophysical journal*, 88(4):2626–2637, 2005.
- [69] Norbert Kučerka, Stephanie Tristram-Nagle, and John F Nagle. Closer look at structure of fully hydrated fluid phase dppc bilayers. *Biophysical journal*, 90(11):L83–L85, 2006.
- [70] Norbert Kučerka, Stephanie Tristram-Nagle, and John F Nagle. Structure of fully hydrated fluid phase lipid bilayers with monounsaturated chains. *The Journal of membrane biology*, 208(3):193–202, 2005.

- [71] Stephanie Tristram-Nagle, Chao-Ping Yang, and John F Nagle. Thermodynamic studies of purple membrane. *Biochimica et Biophysica Acta (BBA)-Biomembranes*, 854(1):58–66, 1986.
- [72] <http://www.basic.northwestern.edu/biotools/proteinCalc.html>.
- [73] A. C. V. Johansson and E. Lindahl. The role of lipid composition for insertion and stabilization of amino acids in membranes. *Journal of Chemical Physics*, 130(18), 2009.
- [74] S. Tristram-Nagle and J. F. Nagle. Hiv-1 fusion peptide decreases bending energy and promotes curved fusion intermediates. *Biophysical Journal*, 93(6):2048–2055, 2007.
- [75] L. B. Li, I. Vorobyov, and T. W. Allen. Potential of mean force and pk(a) profile calculation for a lipid membrane-exposed arginine side chain. *Journal of Physical Chemistry B*, 112(32):9574–9587, 2008.
- [76] I. Vorobyov, L. B. Li, and T. W. Allen. Assessing atomistic and coarse-grained force fields for protein-lipid interactions: The formidable challenge of an ionizable side chain in a membrane. *Journal of Physical Chemistry B*, 112(32):9588–9602, 2008.
- [77] J. L. MacCallum, W. F. D. Bennett, and D. P. Tieleman. Distribution of amino acids in a lipid bilayer from computer simulations. *Biophysical Journal*, 94(9):3393–3404, 2008.
- [78] E. V. Schow, J. A. Freites, P. Cheng, A. Bernsel, G. von Heijne, S. H. White, and D. J. Tobias. Arginine in membranes: The connection between molecular dynamics simulations and translocon-mediated insertion experiments. *Journal of Membrane Biology*, 239(1-2):35–48, 2011.
- [79] W. C. Wimley, T. P. Creamer, and S. H. White. Solvation energies of amino acid side chains and backbone in a family of host-guest pentapeptides. *Biochemistry*, 35(16):5109–5124, 1996.
- [80] W. C. Wimley and S. H. White. Experimentally determined hydrophobicity scale for proteins at membrane interfaces. *Nature Structural Biology*, 3(10):842–848, 1996.

- [81] B. Roux. Lonely arginine seeks friendly environment. *Journal of General Physiology*, 130(2):233–236, 2007.
- [82] W. Kabsch and C. Sander. Dictionary of protein secondary structure: pattern recognition of hydrogen-bonded and geometrical features. *Biopolymers*, 22(12):2577–637, 1983.
- [83] D. Choi, J. H. Moon, H. Kim, B. J. Sung, M. W. Kim, G. Y. Tae, S. K. Satija, B. Akgun, C. J. Yu, H. W. Lee, D. R. Lee, J. M. Henderson, J. W. Kwong, K. L. Lam, K. Y. C. Lee, and K. Shin. Insertion mechanism of cell-penetrating peptides into supported phospholipid membranes revealed by x-ray and neutron reflection. *Soft Matter*, 8(32):8294–8297, 2012.
- [84] K. Huang and A. E. Garcia. Free energy of translocating an arginine-rich cell-penetrating peptide across a lipid bilayer suggests pore formation. *Biophysical Journal*, 104(2):412–420, 2013.
- [85] Martin J Janiak, Donald M Small, and G Graham Shipley. Temperature and compositional dependence of the structure of hydrated dimyristoyl lecithin. *Journal of Biological Chemistry*, 254(13):6068–6078, 1979.
- [86] Haruhiko Yao, Sinzi Matuoka, Boris Tenchov, and Ichiro Hatta. Metastable ripple phase of fully hydrated dipalmitoylphosphatidylcholine as studied by small angle x-ray scattering. *Biophysical journal*, 59(1):252–255, 1991.
- [87] W J Sun, S Tristram-Nagle, R M Suter, and J F Nagle. Structure of the ripple phase in lecithin bilayers. *Proceedings of the National Academy of Sciences*, 93(14):7008–7012, 1996.
- [88] Beth A Cunningham, Ari-David Brown, David H Wolfe, W Patrick Williams, and Anthony Brain. Ripple phase formation in phosphatidylcholine: Effect of acyl chain relative length, position, and unsaturation. *Physical Review E*, 58(3):3662, 1998.
- [89] Kell Mortensen, Walter Pfeiffer, Erich Sackmann, and Wolfgang Knoll. Structural properties of a phosphatidylcholine-cholesterol system as studied by small-angle neutron scattering: ripple structure and phase diagram. *Biochimica et Biophysica Acta (BBA)-Biomembranes*, 945(2):221–245, 1988.

- [90] Jeremy P Bradshaw, Michael S Edenborough, Philip JH Sizer, and Anthony Watts. Observation of rippled dioleoylphosphatidylcholine bilayers by neutron diffraction. *Biochimica et Biophysica Acta (BBA)-Biomembranes*, 987(1):111–114, 1989.
- [91] JT Woodward IV and JA Zasadzinski. Amplitude, wave form, and temperature dependence of bilayer ripples in the p  $\beta$  phase. *Physical Review E*, 53(4):R3044, 1996.
- [92] M. P. Hentschel and F. Rustichelli. Structure of the ripple phase  $P'_\beta$  in hydrated phosphatidylcholine multimembranes. *Phys. Rev. Lett.*, 66:903–906, Feb 1991.
- [93] John Katsaras, Stephanie Tristram-Nagle, Yufeng Liu, RL Headrick, E Fontes, PC Mason, and John F Nagle. Clarification of the ripple phase of lecithin bilayers using fully hydrated, aligned samples. *Physical Review E*, 61(5):5668, 2000.
- [94] Li Li and Ji-Xin Cheng. Coexisting stripe-and patch-shaped domains in giant unilamellar vesicles. *Biochemistry*, 45(39):11819–11826, 2006.
- [95] Alex H. de Vries, Serge Yefimov, Alan E. Mark, and Siewert J. Marrink. Molecular structure of the lecithin ripple phase. *Proceedings of the National Academy of Sciences of the United States of America*, 102(15):5392–5396, 2005.
- [96] S. A. Tristram-Nagle. Preparation of oriented, fully hydrated lipid samples for structure determination using x-ray scattering. *Methods Mol Biol*, 400:63–75, 2007.
- [97] [http://henke.lbl.gov/optical\\_constants](http://henke.lbl.gov/optical_constants).
- [98] M.C. Wiener, R.M. Suter, and J.F. Nagle. Structure of the fully hydrated gel phase of dipalmitoylphosphatidylcholine. *Biophysical Journal*, 55(2):315 – 325, 1989.
- [99] Kheya Sengupta, V. A. Raghunathan, and John Katsaras. Structure of the ripple phase of phospholipid multibilayers. *Phys. Rev. E*, 68:031710, Sep 2003.
- [100] J. Katsaras and V. A. Raghunathan. Molecular chirality and the ripple phase of phosphatidylcholine multibilayers. *Phys. Rev. Lett.*, 74:2022–2025, Mar 1995.

- [101] Alejandro B. Rodriguez-Navarro. Registering pole figures using an X-ray single-crystal diffractometer equipped with an area detector. *Journal of Applied Crystallography*, 40(3):631–634, Jun 2007.
- [102] Jessy L. Baker, Leslie H. Jimison, Stefan Mannsfeld, Steven Volkman, Shong Yin, Vivek Subramanian, Alberto Salleo, A. Paul Alivisatos, and Michael F. Toney. Quantification of thin film crystallographic orientation using x-ray diffraction with an area detector. *Langmuir*, 26(11):9146–9151, 2010. PMID: 20361783.